The Nanomechanical Behaviour of The Human Annulus Fibrosus

By

Radhwa Yumna Ginting

Thesis
Submitted to Flinders University
for the degree of

Master of Biomedical Engineering

College of Science and Engineering

17 November 2023

TABLE OF CONTENTS

DECLARATION

I certify that this thesis:

1. does not incorporate without acknowledgment any material previously submitted for a degree or diploma in any university

2. and the research within will not be submitted for any other future degree or diploma without the permission of Flinders University; and

3. to the best of my knowledge and belief, does not contain any material previously published or written by another person except where due reference is made in the text.

Signature of student..

Print name of student.....Radhwa Yumna Ginting.....

Date.......17 November 2023..........

I certify that I have read this thesis. In my opinion it is/is not (please circle) fully adequate, in scope and in quality, as a thesis for the degree of Master of Biomedical Engineering. Furthermore, I confirm that I have provided feedback on this thesis and the student has implemented it minimally/partially/fully (please circle).

Signature of Principal Supervisor...

Print name of Principal Supervisor   John Costi

Date..........17/11/2023.........................

ACKNOWLEDGEMENTS

ABSTRACT

The degeneration of the intervertebral disc (IVD) is a prevalent musculoskeletal condition that commonly presents as low back pain. The development of more effective treatments may be facilitated by a greater understanding of the mechanisms underlying disc degeneration. The Annulus Fibrosus (AF) is a structural component primarily composed of type I collagen which plays a significant role in the disc's reaction to mechanical loading. To achieve a more thorough examination of the disc and accurately identify the impact of disc degeneration on different anatomical regions within the disc, it is critical to investigate the mechanical properties of the disc at the nanoscale. This can be accomplished by studying collagen type I fibrils extracted from the AF fibre bundles obtained from circumferential sections of both healthy and degenerated discs under ambient conditions and become the main focus of this study. The study involved the isolation and examination of the nanomechanical characteristics of the circumferential regions of both healthy and degenerated discs. A comparison was made between two specific circumferential regions within the disc namely the anterior lateral and posterior regions. The idea of this comparison was to evaluate the structure and Young's modulus of the individual fibril by subjecting them to the same load. Following a 30-minute thawing time at room temperature, the fibrils would undergo testing after being removed from the Phosphate Buffered Saline (PBS) solution. To determine the topographical and mechanical properties of the sample, the Bruker Multimode 8 instrument engages in physical interaction with the cantilever tip positioned between the probe and the specimen during the scanning process of the collagen fibrils' surface. The calculation of Young's modulus is performed by the utilisation of the Hertz model. The results of the study indicate that the Young's modulus is greater in the anterior lateral sections in comparison to the posterior parts. Additionally, it was observed that degenerated discs had an apparent influence on the increased Young's modulus value when compared to the healthy discs. The comprehensive evaluation of the study's findings is important due to the limited sample sizes and limits imposed by the testing apparatus. Future research should consider evaluating collagen fibrils in a thoroughly hydrated environment to imitate the physiological condition more effectively and to provide additional clarity, particularly in the posterior region.

LIST OF FIGURES

LIST OF TABLES

1. INTRODUCTION

Low back pain is the primary cause of years lost to disability on a global scale and its prevalence is increasing in tandem with the ageing and expansion of the population (Feigin, 2016). Back pain plays a significant role in illness, disability, and discomfort ranking as the second most common cause of disease burden in Australia. According to the Australian Institute of Health and Welfare (AIHW, 2023), back pain and its associated issues were the primary contributors to the economic burden caused by diseases comprising 4.2% of Australia's overall disease burden. It imposes a financial burden of around $3.4 billion annually on the health system which is equivalent to 2.4% of the overall health expenditure (AIHW, 2023). The preceding data strongly suggest that the socioeconomic impact of lower back pain is significant affecting approximately one in six individuals within the country. This impact is mostly observed through increased hospitalisation rates and decreased production levels. Low-back pain is classified as a musculoskeletal condition and one potential cause is the degeneration of intervertebral discs (IVDs).

The spine offers the structural stability and flexibility required for the preservation of posture and trunk mobility. The biggest avascular, multi-regional structures that are situated between the vertebral bodies of the spine are known as IVDs, and they are the subject of this study. The IVDs of the human lumbar spine has a complicated morphology and structure which is consistent with its primary functions are to permit motion between absorbing shock, adjacent vertebral bodies, and transmitting loads through the vertebral column (Pham, 2015). The IVDs are fibrocartilage pads between spine vertebrae and comprised of two distinct anatomical regions which are the Nucleus Pulposus (NP) and the Annulus Fibrosus (AF). From the vertebral end plates, the AF protrudes and encircles the nucleus. Water accounts for approximately 60% of the AF, along with cells (fibroblasts and chondrocytes), elastin, and proteoglycans (Buckwalter, 1995; Cassidy et al., 1989).
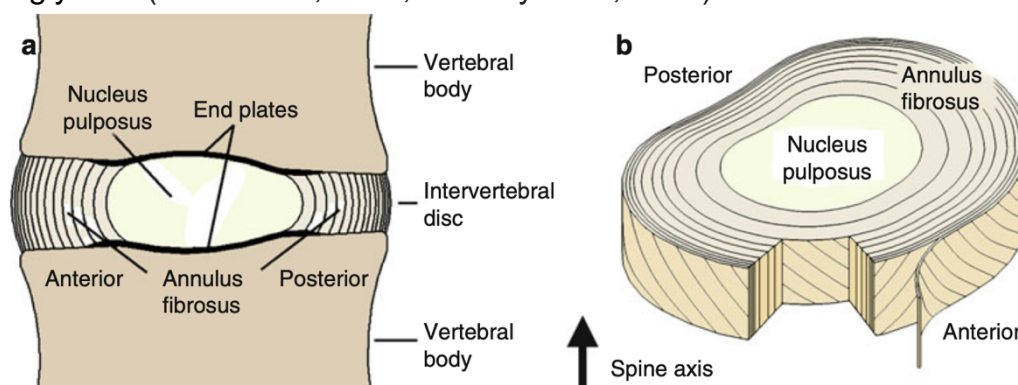
Figure 1. Schematic illustrations of the structure and components of the IVD showing anatomical regions from midsagittal cross section (a) and the structure of lamellar in AF (b) (Smith et al., 2011)

The IVDs are especially susceptible to age-related alterations due to their limited regeneration and repair capacity (Adams, 2015). Disc function declines with age, this age-related changes in disc composition make it susceptible to structural disruptions like disc herniation or slipped disc, which can cause degeneration, discomfort, and disability (Adams, 2015). The terms "degenerated discs," "disc disease," "herniated discs," and "slipped discs" are frequently used to describe low back discomfort which is sometimes referred to as a musculoskeletal illness and which causes IVD to degenerate (Lewis et al., 2008; Pham, 2015). Concentric and radiating tears, reduction in height of the disc, reduction of distinction from the AF, thickening of the lamellae, gradually fibrous alteration within the NP from gelatinous to fibrotic, absence of the organisation of annular lamellae, and progressive elimination of the vertebral endplate represent a number of the effects of the degeneration of the disc (Osti et al., 1992).

The AF is one area that significantly affects the disc's loading response which is located in the IVD's outer fibrous layer, protrudes from the vertebral end plates and encircles the NP, a soft, extremely hydrophilic substance that resembles gel (Hang & Barber, 2011; Pham, 2015). The AF consists of a number of nearly circumferential layers known as lamellae (Cassidy et al., 1989). The mechanical properties of the AF which include anisotropy and nonlinearity are a result of its composition and highly organised structure (O'Connell et al., 2009). Collagen has a crucial role in providing structural support to both the AF and the IVDs. The formation of a compact network of fibres has a crucial role in preserving the structural arrangement and mechanical resilience of the IVDs. Collagens exhibit inherent high tensile strength mostly attributed to the presence of intermolecular covalent crosslinks. These crosslinks are initially reducible during the early phases of fibril production but gradually stabilise as the tissue grows.

The most abundant protein in the AF, collagen type I, has a complex and hierarchical structure that extends from the molecular to the aggregate level and the foundation of connective tissue which is made up of intervertebral discs, skin, bone, cartilage, ligaments, tendons, and other tissues (Graham et al., 2004; Gutsmann et al., 2004; Ottani et al., 2002). Because of this, it has the potential to maximise its behaviour and mechanically adjust at each structural level and is therefore likely to play a significant role in the disc's overall function (Fratzl, 2008).

Collagen type I fibres are organised in concentric lamellae to form the AF which surrounds the nucleus (Bogduk, 2005). The outer part of AF is predominantly comprised of type I

collagen and represents the area with the highest concentration of collagen (Filanowski et al., 2003). The bundles of collagen fibres are encased in each lamella's ground matrix. Additionally, there is an observed increase in the fraction of collagen type I ranging from 0% to 100%, as the distance in the radial direction from the nucleus increases (Schollmeier et al., 2000). The collagen fibres within the outer AF are firmly attached to the surrounding vertebral bodies, whereas in the inner AF, they exhibit a circular arrangement around the NP progressively merging into the cartilage endplate. The AF contains collagen fibres that possess a planar zig-zag arrangement commonly referred to as crimped structure. This particular arrangement allows the fibres to go through more elongation by straightening out the crimps (Adams, 2015). The structural arrangement of the collagen fibril within the AF is shown in the figure 2.
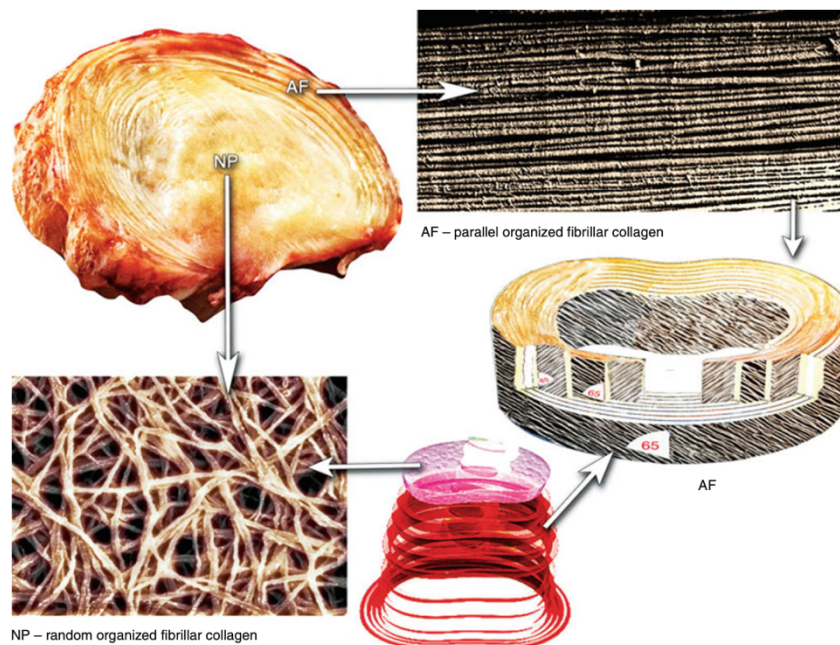
Figure 2. The illustration of the structural arrangement of fibrillar collagens within the AF and NP of the IVD in human (Cortes & Elliott, 2014)

The IVD's mechanical characteristics at lower hierarchical levels at the nanoscale is crucial to give a more thorough, smaller-scale study of the disc and to elucidate the impact disc degeneration may have had upon the various components inside the disc. The focus of this study is on the nanoscale behaviour of collagen type I fibrils that were removed from the AF fibre bundles. The circumferential sections of the AF were examined in order to learn more about the collagen type I fibrils that form the AF lamellae. Samples of both healthy and degenerative human discs were taken from the anterior-lateral (ALT) and posterior (PST) region of the disc which utilised to investigate for individual collagen type 1 fibrils.

2. LITERATURE REVIEW

The intervertebral disc (IVD) holds significant importance within the human musculoskeletal system. This topic has received substantial research interest throughout over a period of time rendering it a subject of extensive investigation. Collagen has a crucial role in providing structural support to both the annulus fibrosus (AF) and the IVD. Hence, it is crucial to investigate the mechanical characteristics of collagen type I fibrils inside the human AF at the nanoscale.

This study is intended to clarify the underlying reasons for the observed regional variations in mechanical properties at a higher structural level and to identify the specific stage at which disc degeneration becomes detectable. This research intends to enhance our comprehension of the contribution of hierarchical level to the overall functioning of the AF. Additionally, it seeks to provide valuable insights that can enhance our understanding of disc degeneration, thereby facilitating the advancement of more efficacious treatment methodologies.

2.1 Collagen type 1 fibril

Collagen type I has been demonstrated to possess viscoelastic characteristics and a notable degree of tensile strength. It serves as the primary structural component of the AF and plays a significant role in conferring its remarkable resilience and ability to withstand tension (Bogduk, 2005; Junqueira & Carneiro, 2005). The components that constitute each level of the collagen hierarchy exhibit significant variations in size and can present challenges in terms of precise definition (Fratzl, 2008; Pham, 2015).

At the supramolecular level of collagen's structure, the aggregation of tropocollagen molecules gives rise to the formation of microfibrils. Microfibrils exhibit lateral and longitudinal aggregation resulting in the formation of fibrils. Covalent crosslinks have a crucial role in stabilising the inter microfibrillar structure. Tropocollagen molecules exhibit a parallel arrangement with five molecules aligned side by side and are longitudinally distributed in a quarter-staggered configuration which are interconnected through covalent crosslinks highlighted in green and black to denote their respective locations shown in figure 3b. These entities constitute a microfibril with a diameter of 3.5 nm (Viidik, 1973).

The thickness of the fibrils typically fall between 50 and a few hundred nanometres and the mechanical characteristics of the tissues are mostly influenced by the structural

arrangement of the collagen fibrils (Balasubramanian et al., 2013). The presence of the quarter-stagger array is a notable structural attribute as it is responsible for the distinctive 67 nm banding pattern observed in all fibrous collagens (Heim et al., 2006; Van Der Rijt et al., 2006). This D banding value is consistent with the findings of a study conducted by Erickson et al. (2013) which indicated that collagen type I molecules have D-periodicity ranging from 60-73 nm. When observed in lateral view, there are regions of approximately 35 nm characterised by gaps, as well as regions of approximately 32 nm characterised by overlaps. The described patterns are representative of the distinctive bright and dark stripes as depicted in figure 3c.

The diameter of fibrils can vary between 50 and 500 nm contingent upon the specific location of the collagen (Fratzl, 2008). In the study conducted by Kontomaris et al. (2022), it was observed that the collagen molecule had a length of 300 nm and a diameter of 1.6 nm. This finding provides confirmation that the diameter of fibrils might exhibit variability. The size of collagen fibrils is significantly smaller in comparison to human hair with individual hair strands on the human scalp having a thickness ranging from 40 to 120 micrometres (Robbins, 2002).
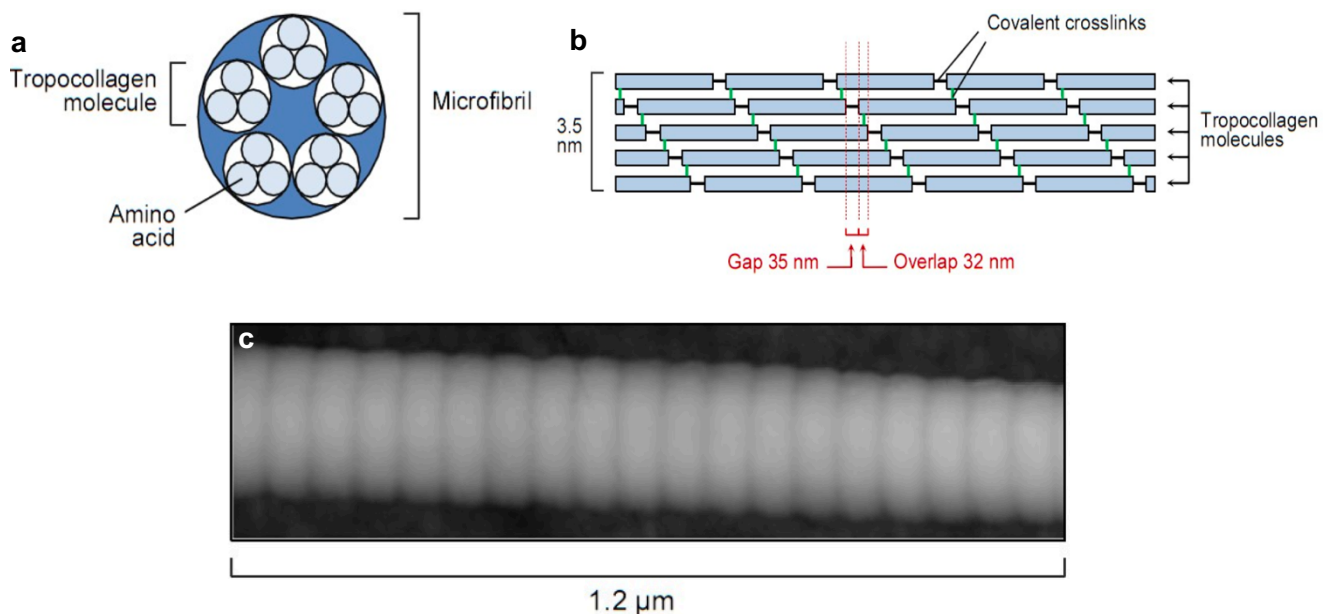
Figure 3. The structure of collagen microfibrils displays a cross-sectional perspective of a microfibril (a) and a lateral view of a quarter-stagger arrangement of tropocollagen molecules (b) (Pham, 2015; Van Der Rijt et al., 2006) and an atomic force microscope (AFM) image capturing the structure of a collagen microfibril (c) (Heim et al., 2006)

2.2 Nanomechanical Testing and Collagen Fibril Mechanical Properties

The Atomic Force Microscopy (AFM) is a microscope with a scanning probe that is used for the examination of the surface structure, properties, and mechanical characteristics of

the samples at the nanoscale level in a wide range of applications. Other apparatus methods such as Brillouin spectroscopy (Cusack & Miller, 1979; Harley et al., 1977), data from X-rays (Sasaki & Odajima, 1996), force spectroscopy (Sasaki & Odajima, 1996; Van Der Rijt et al., 2006), microelectromechanical systems (MEMS) (Eppell et al., 2006; Shen et al., 2008; Shen et al., 2011), and steered molecular dynamics simulations of tropocollagen-like molecules (Lorenzo & Caffarena, 2005) have all been used to investigate the mechanical properties of each of the collagen fibrils.

The AFM operates by utilising the interaction between a finely pointed probe tip and the sample by scanning the sample's surface using the probe tip. By determining the forces and deflections that arise as the tip interacts with the sample, valuable information regarding the sample's mechanical and topographical properties can be inferred. As a result, the AFM can resolve objects as fine as 2 nm (Bruker, 2010) which makes it ideal for investigating collagen type 1 fibrils. Because of its high potential for use in real-world clinical settings, AFM nanoindentation has emerged as the main technique for characterising biological specimens at the nanoscale (Hang & Barber, 2011; Stylianou et al., 2019; Svensson et al., 2010).

Research by Kontomaris et al. (2022) examined alternative interaction mechanics concepts to interpret force-indentation datasets depending on predictions about the form of the indenter tip and fibrils of collagen along with the elasticity or elasticity-plastic interaction assumption. Throughout the past two decades, there has been a strong scientific enthusiasm for accurately determining the Young's modulus of collagen fibrils utilising AFM nanoindentation (Kontomaris et al., 2022). The observed values of Young's modulus in the scientific literature, nevertheless, differ greatly. For instance, Wenger et al. (2007) used the Oliver and Pharr methodology by using sphere-elastic half-space contact to compute the Young's modulus of collagen type 1 fibrils tendon from rat tail. Their values ranged from 5 to 11.5 GPa (Wenger et al., 2007). The Young's modulus calculated for dry collagen fibrils ranges from 0.9 - 11.5 GPa (Kontomaris et al., 2022). For dry fibrils, Young's modulus was 1.9 ± 0.5 GPa, and for fibrils in buffer solution, it was 1.25±0.1 MPa (Grant et al., 2008). Grant et al. (2008) calculated the Young's modulus of collagen type 1 fibrils derived from the tendon of the bovine Achilles using sphere-sphere interaction by the mechanism of Hertzian.

The study conducted by (Pham, 2015) examined the Young's modulus of individual collagen fibrils within the human AF across four distinct sections of the IVDs using Hertz model of AFM nanoindentation, namely the anterior (A), anterior lateral (AL), lateral (L), and posterior lateral (PL) regions. The findings of the study indicate that the mean young's

6

modulus together with its 95% confidence interval, did not exhibit a significant impact from the degenerative grade in both healthy and degenerate extracted collagen fibrils. The observed values for the young's modulus were within the range of 2.5 GPa (Pham, 2015). In 2007, similar study using the same Hertz model by (Strasser et al., 2007) conducted investigating the elastic properties of individual collagen type I fibrils. This investigation utilised AFM nanoindentation to analyse native collagen fibrils on the outer shell and within the core of the fibril. The indentation experiments conducted on both the shell and core of dissected collagen fibrils unable to confirm the presence of distinct Young's moduli for the core and shell regions. The mean values were computed to be roughly 1.2 GPa (Strasser et al., 2007).

2.3 Gaps in the Literature

Extensive research has been conducted in the scientific literature on the nanoscale properties of collagen due to its relevance to important medicinal applications. However, there is a limited availability of collagen properties studies derived from the AF of the human IVD particularly in relation to the posterior part. In 2015, Dr. Pham conducted a notable investigation on the nanomechanical properties of the AF across four distinct anatomical regions: anterior, anterolateral, lateral, and posterolateral. However, it is important to note that the study did not include analysis of the AF in the posterior region. Hence, the primary objective of this work is to further our understanding of the nanomechanical characteristics of the AF collagen type 1 in the human IVD, specifically focusing on the impact of degeneration in the posterior region of the IVD.

3. METHODOLOGY

The human IVDs from 3 healthy and 5 degenerated discs were obtained from the Biomechanics and Implants Laboratory located at Flinders University, Tonsley. This study degeneration grading of the disc as healthy or deteriorated using the commonly used Thompson criteria (Thompson et al., 2000). A prevalent five-point scale used for grading is based on the nucleus, annulus, vertebral endplates, and vertebral body. Three of the discs in the sample were classified as grade 2 indicating a healthy condition, while the remaining five discs were classified as grade 4 indicating degeneration (Table 1). The samples collected from 19- to 90-year-old human cadaveric spines. However, due to limitations in this study, only one grade 2 disc and two grade 4 discs were able to undergo testing. The following sample preparation and collagen extraction procedures employed in this study were adapted from the thesis of Dr Pham (2015).

Table 1. Human isolated discs were collected from various levels of the lumbar spine. These discs were then assessed and classified based on the Thompson scale with the area of interest are ALT and PST regions.

Sample Number	Grade	Level	Age / Gender	Region Taken
GL191447	2	L2-L3	34 / M	ALT and PST
GL864	2	L2-L3	65 / M	ALT and PST
4696	2	L5-S1	58 / M	ALT and PST
5194	4	L2-L3	55 / M	ALT
5194	4	L4-L5	55 / M	PST
GL471	4	L4-L5	65 / M	ALT and PST
5029	4	L4-L5	49 / F	ALT
GL463	4	L4-L5	54 / M	PST

3.1. Isolation of the disc

This study preliminary conducted practise experiments on sheep IVD samples obtained from sheep functional spine units (FSU) in order to gain familiarity with the process of isolating the disc. This initial step was taken prior to proceeding with the isolation of human discs. The utilisation of sheep as a substitute for cadaver material in spine research has been growing due to the challenges associated with acquiring human cadavers. The

research conducted by Wilke et al. (1997) reveals that there exist biomechanical correlations between the spines of sheep and humans. The height and lateral diameter of the human lumbar disc typically measure between 12.5 and 45 mm (Bogduk, 2005), respectively, although these characteristics may vary among individuals. In a study conducted by (O'connell et al., 2006), it was observed that the normalised disc height of humans measured 8.93 mm, whereas in sheep, it measured 2.61 mm. Additionally, the disc area in humans was found to be 1727 mm, whereas in sheep, it measured 344 mm. The posterior part of the ovine disc exhibited an insufficient in height resulting in the inability to section the identified AF using a handheld microtome.

In this experimental study, the IVDs have been defined inside the specified locations as illustrated in Figure 4. The regions are known by their abbreviations as anterior (ANT), anterior lateral (ALT), lateral (LAT), posterior lateral (PLT), and posterior (PST). The disc, which was initially isolated, was subsequently divided into distinct areas and placed in a tiny container. However, prior to being put in the airtight small container with the labelled name as depicted in Figure 3, the segmented discs required wrapping with hydrated gauze that had been sprayed with PBS followed by the application of plastic wrap. The samples are stored in the Biomechanics lab freezer in the temperature of -20°C until the day of testing.
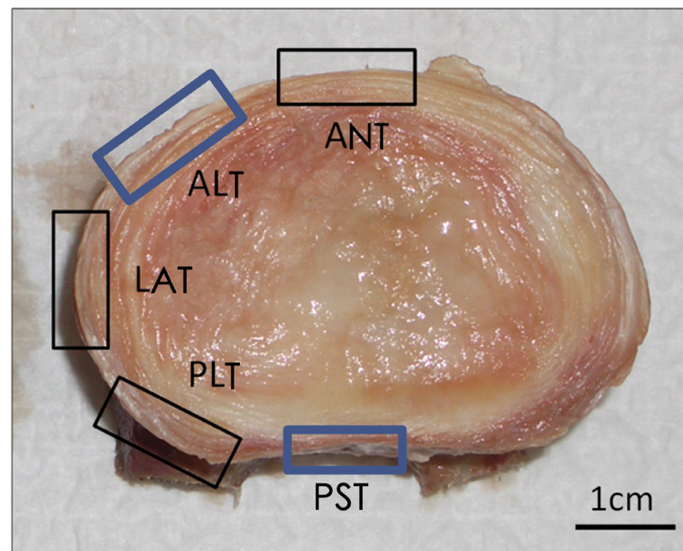
Figure 4. The dissected disc illustrating five distinct anatomical regions: anterior (ANT), anterior lateral (ALT), lateral (LAT), posterior lateral (PLT), and posterior (PST). Two specific locations of concern are highlighted within the image using blue boxes (Pham, 2015).
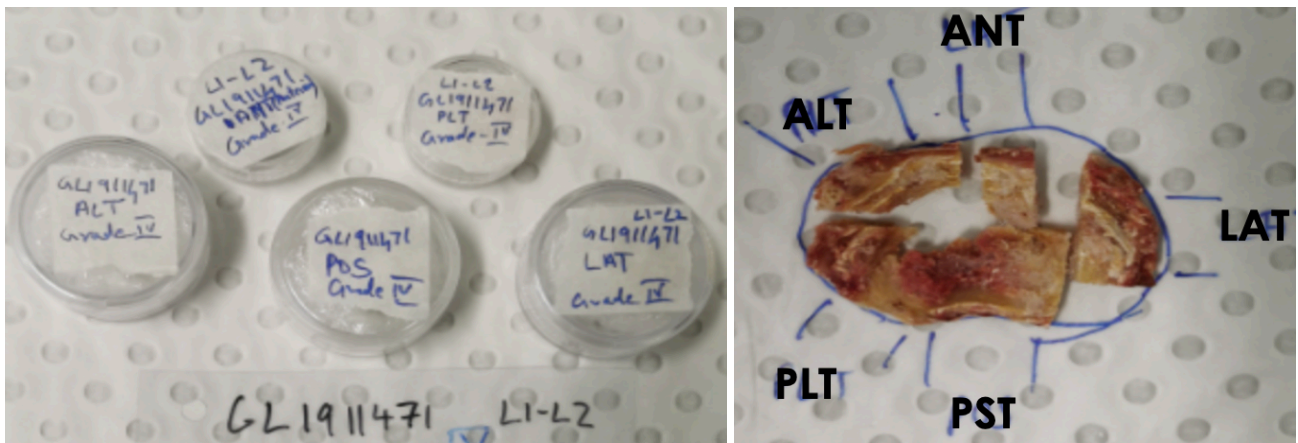
Figure 5. The segmented areas from the isolated disc showing from the human AF

3.2. Extraction of the collagen fibres

The segmented discs are thawed for around 30 minutes before being retrieved for the collagen fibres. To extract the collagen fibres, a method similar to that employed by Dr Pham's thesis was utilised. However, in order to facilitate the process of teasing out the fibres, the segmented disc was sliced into 1 mm thickness with a width of 5 mm using a hand microtome. The samples were carefully positioned on a metal plate measuring 5cm in length in order to create an easily discernible divide between the layers. This was achieved by using teasing needles and a pair of small surgical tweezers. Furthermore, a light microscope at Flinders Medical Centre (FMC) was utilised to enhance visibility and facilitate the extraction of collagen fibres as shown in Figure 6.

Given that the only way to see individual collagen fibril is with AFM imaging, the samples are observed under an Olympus Brightfield BX53 Upright Microscope until the strands of the collagen can be seen as shown in the figure 5. The samples shown in the figure 6d with scalebar of 100 µm under 20x. The fibres were extracted from the centre of the sample. Subsequently, the fibres were deposited onto recently split (freshly cleaved) mica (substrate or testing base for AFM) that were attached to metal pucks using double-sided tape. The fibres were allowed to dry for about ten minutes, after which two opposing sides were painted with a thin coat of nail varnish keeping a 0.5–1.0 mm wide unpolished strip running along the middle of the puck (Pham, 2015) as shown in the figure 6. The primary objective of applying varnish was to secure the adhesion of the fibres to the mica substrate.
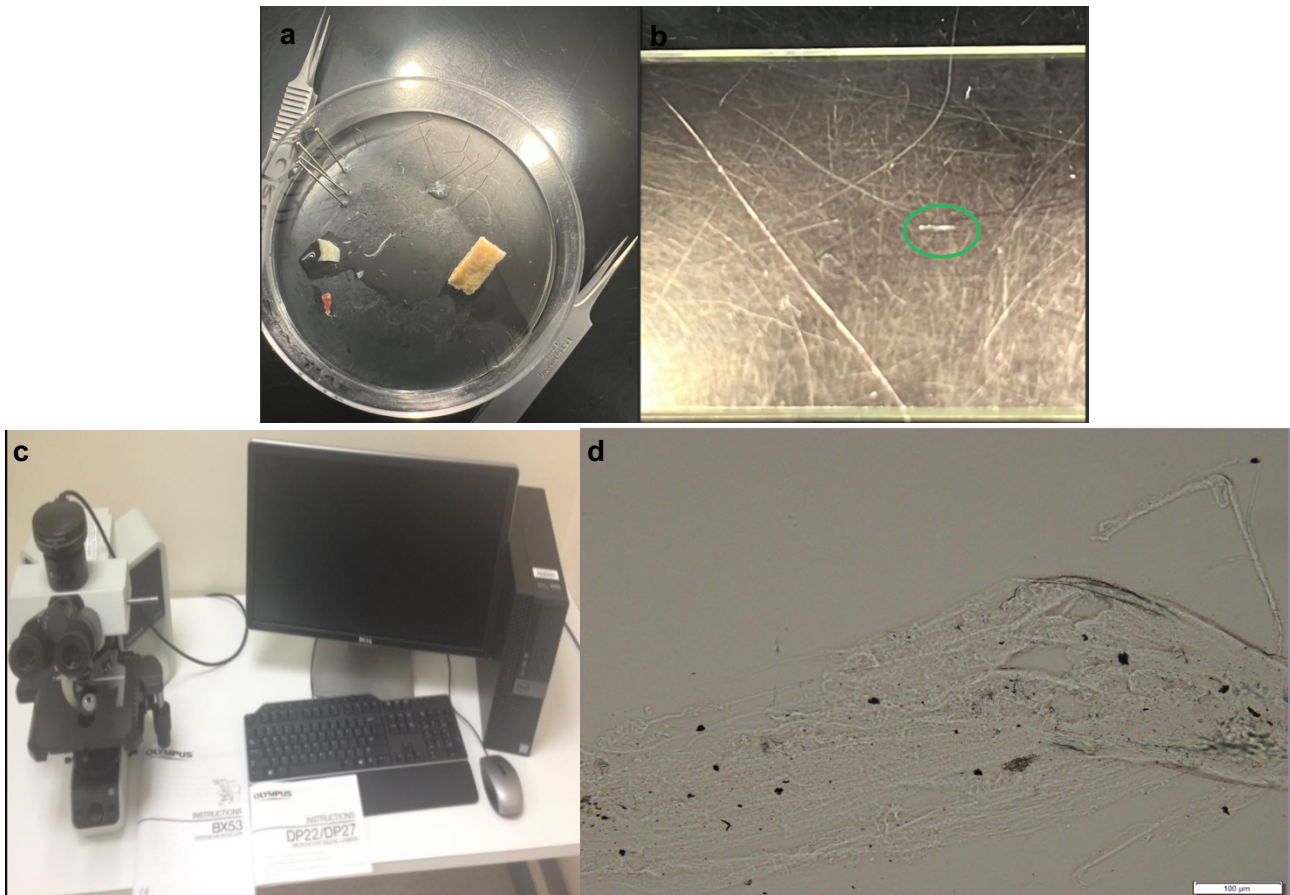
Figure 7. The bundles were extracted (a) and subsequently elongated into a thin, small, and flat fibre (b) which was subsequently examined under the Olympus Brightfield BX53 Upright Microscope (c) to identify the strands of collagen (d)
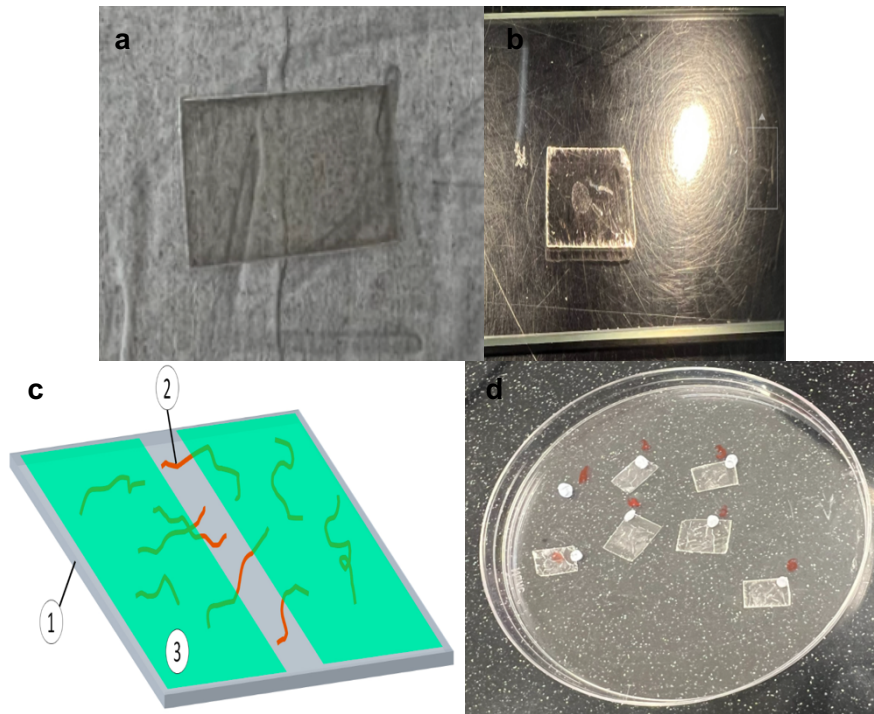
Figure 8. The mica (a) freshly cleaved before depositing the fibrils onto it (b). The surface of the mica was coated with a layer of varnish observed on the sides of the mica leaving a distinct gap in the middle (c) (Pham, 2015): 1 shows the mica surface, 2 shows the collagen fibres and 3 shows the varnish. The samples then ready to be tested (d)

3.3. AFM Testing

In this study, we used NanoScope V Controller equipment from Bruker Corporation in Massachusetts, USA. This Bruker MutiMode 8 scans the collagen fibrils' surface by doing the physical interactions with the cantilever tip between the probe and the specimen. This study employed two methods namely topographical imaging to visualise the structure of collagen fibrils and force spectroscopy to investigate their mechanical properties at the individual collagen fibril. Bruker MutiMode 8 is able to analyse tiny objects such as 2 nm (Bruker, 2010).
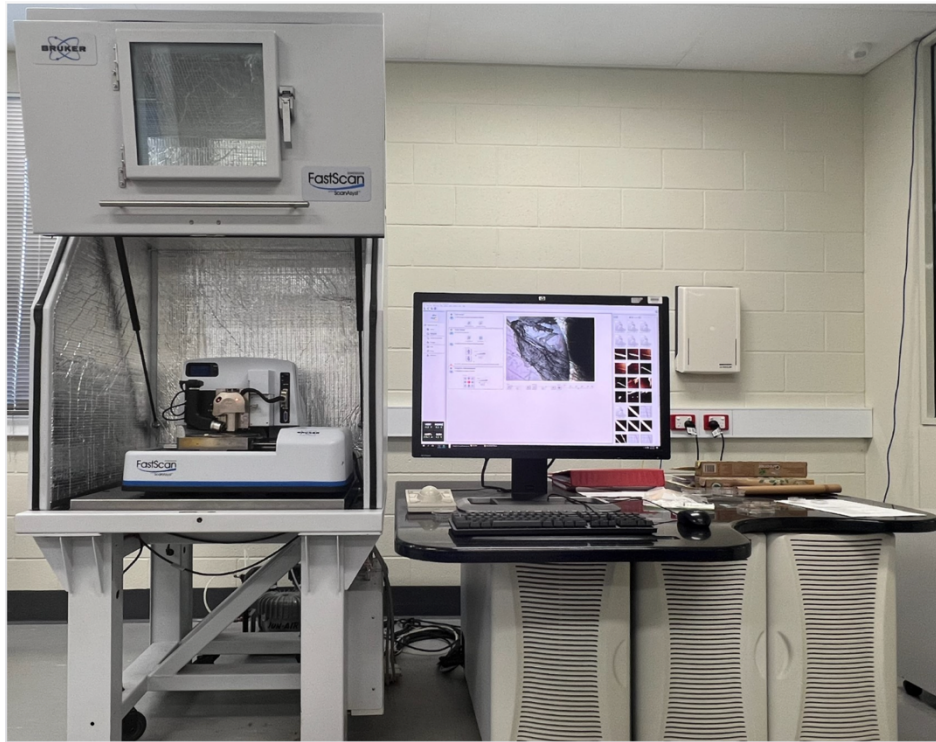
Figure 9. The Bruker MultiMode 8 with Nanoscope V Controller

3.3.1. Topographical Imaging

Topographical imaging is employed for the goal of visually characterising samples resulting in the production of a two dimensional or three-dimensional representation of the surface. The acquisition of the topographic image of the sample involves the representation of the deflection of the cantilever as a function of its position on the sample. In an alternative approach, one may consider graphing the vertical displacement of the translation step. The regulation of height in this context is governed by a feedback mechanism that ensures a consistent force is maintained between the tip and the sample (Butt et al., 2005). The tapping (intermittent) technique was employed in this study. In the tapping mode, the tip exhibits periodic contact with the sample, in contrast to the constant contact observed in the contact mode. While the tip was elevated above the surface, it oscillated with a specific amplitude at its resonant frequency. The magnitude of oscillation reduced when the tip made contact with the surface (Pham, 2015).

The scanning probe was raster-scanned across the surface using a contact mode approach. The probe was then brought into contact with the surface until the oscillation amplitude decreased to a predetermined amplitude set point which was defined as 80% of the initial amplitude (Pham, 2015). The controller effectively maintained the amplitude set point enabling the tip to lightly contact the surface during image acquisition. The force

exerted on the surface was determined by the amplitude set point. For instance, a higher amplitude set-point results in a reduction of the force applied to the surface. This study involved the creation of tapping mode images using height and amplitude data that quantified the deviation in amplitude compared to the set-point amplitude, and phase data that determined the oscillation phase of the cantilever relative to the piezo drive signal. Through the utilisation of topographical imaging techniques, it becomes possible to quantitatively assess many characteristics of the particular collagen fibril including d banding, depth, and width.
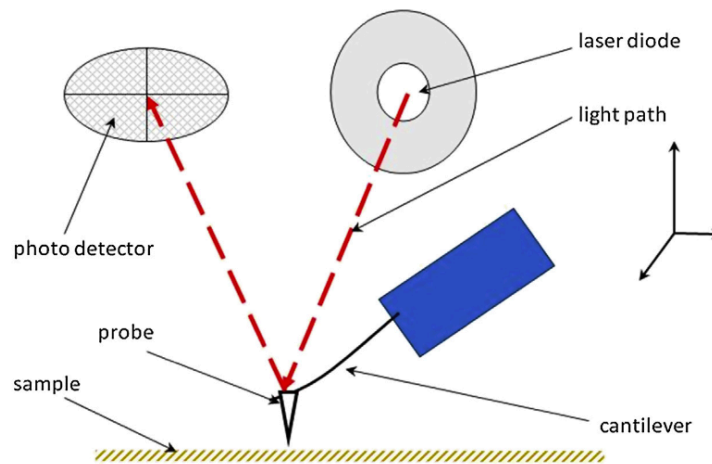
Figure 10. The standard arrangement of AFM (Johnson et al., 2017)

3.3.2. Force Spectroscopy

Force spectroscopy involves the deduction of material properties of a sample through the analysis of dynamic interactions between a tip and the object. This study employed the technique of nanoindentation which is based on the analysis of force curves. A force curve refers to a graphical representation depicting the magnitude of the force exerted on the cantilever when it makes contact with the surface of the sample as shown in the figure 11. Fundamentally, it serves as a depiction of the interaction between the tip and surface, yielding diverse mechanical, chemical, and electrostatic characteristics including adhesive force and elasticity. The tip is first positioned above the sample at a predetermined distance known as the ramp size as set by the user. Under normal circumstances where there is no long-range attraction or repulsion, the cantilever undergoes no deflection (Butt et al., 2005; Cappella & Dietler, 1999; Pham, 2015).
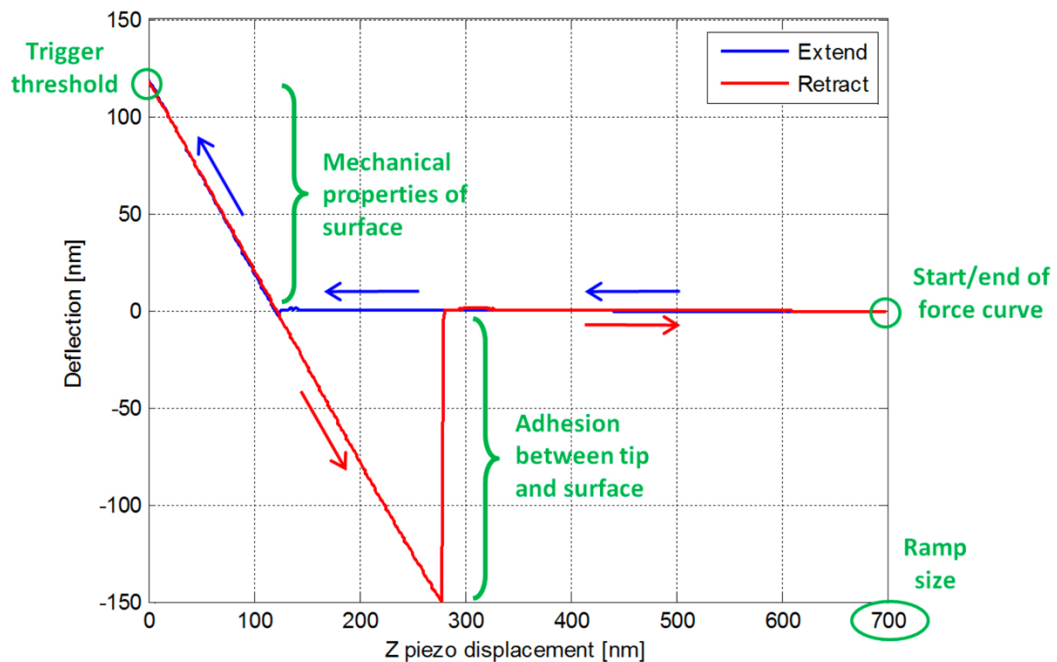
Figure 11. The force curve illustrates the relationship between the corresponding deflection of the tip vs z displacement (Pham, 2015)

The distance between the AFM tip and the sample is altered, while simultaneously detecting and recording the location of the cantilever (specifically, its deflection in the z direction). The deflection refers to the quantification of the force exerted between the surface of the sample and the pointed tip of the probe. The force data can be derived from the deflection data. The force can arise either from direct contact between the surface of the sample and the tip or it can be facilitated by the mechanical interaction of a molecule or another object that is connected at one end to the specimen's surface and at the opposite end to the probe tip. Additionally, it is possible for mediation to occur via a force field such as an electric or magnetic field. The operating procedures involved in AFM force measurement exhibit considerable uniformity across many applications, hence providing the AFM with distinctive use as a force measurement instrument. The force data yields insights into the characteristics of the sample under investigation, as well as occasionally offering details on the properties of the probe being utilised (Serry, 2005).
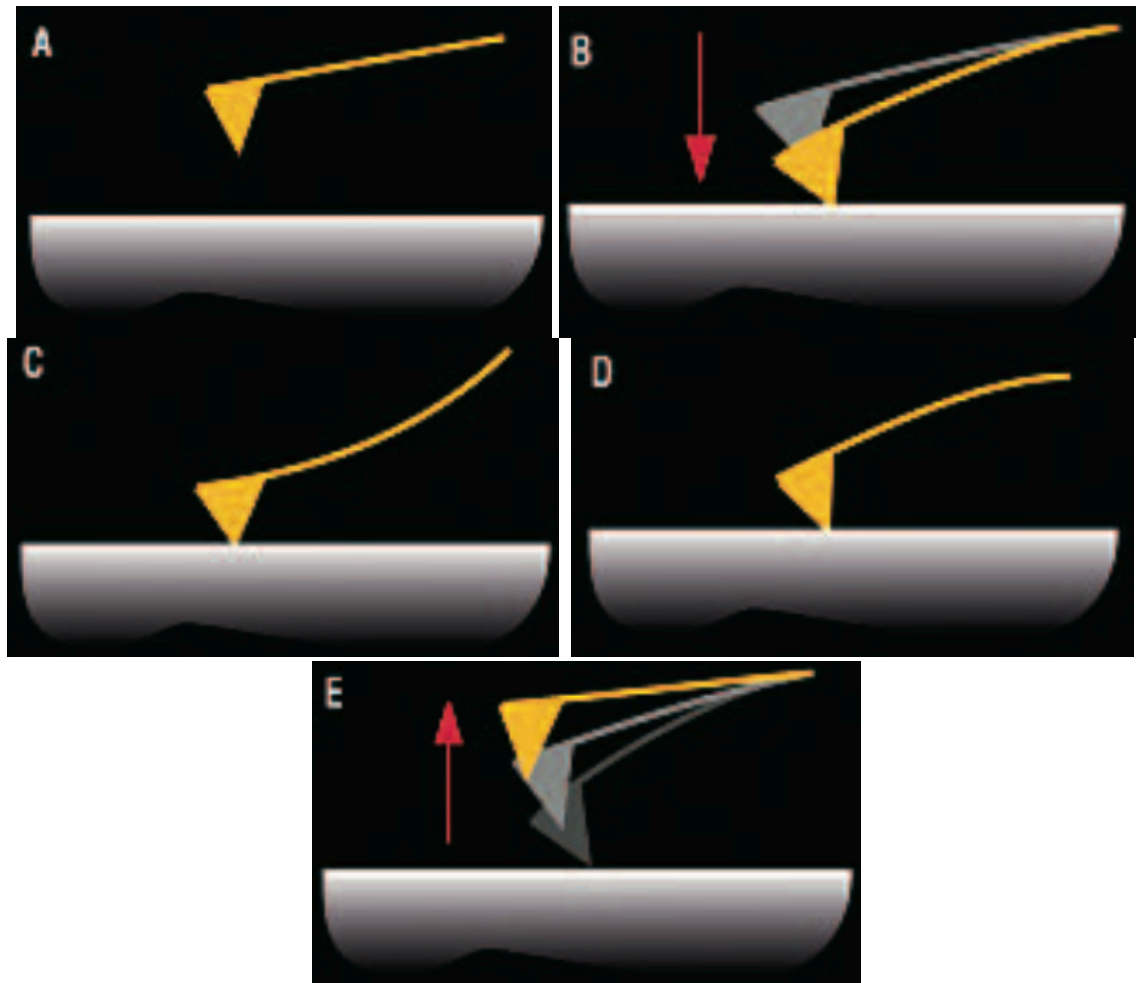
Figure 12. The illustrations of tip and surface interactions (Serry, 2005)

The AFM alters the distance between the probe and the surface of the sample either by extending the sample towards the probe or by extending the probe towards the sample at the base of the cantilever. Simultaneously, the AFM is capable of detecting and graphically representing the movement which is often occurring at or near the end of the cantilever. When the tip approaches the sample surface but is still at a distance where it cannot detect any force exerted by the sample's surface, the cantilever remains in an undeflected state maintaining its equilibrium position. When the tip approaches the sample surface and experiences attraction forces, it causes a tiny downward bending of the cantilever as shown in the figure 12b. The cantilever undergoes upward bending when the AFM maintains movement of the sample or cantilever, causing the tip to exert increased pressure against the sample's surface as shown in the figure 12c. Conversely, the cantilever experiences downward bending when the AFM initiates retraction, separating the cantilever and sample, while the tip remains adhered to the sample as shown in the figure 12d. Ultimately, the tip becomes detached from the surface as shown in the figure 12e leading to the restoration of the cantilever to its state of balance as shown in the figure 12a (Serry, 2005).

If sufficient force is applied to the tip during the force curve process, it is possible to achieve nanoindentation of the surface as shown in the figure 13b. The utilisation of this function holds significant importance within the scope of this research as it allows for the incorporation of nanoindentation data into an equation or model of choice. In this study, the Hertz Model was employed as the preferred model enabling the indirect determination of the sample's young's modulus value.
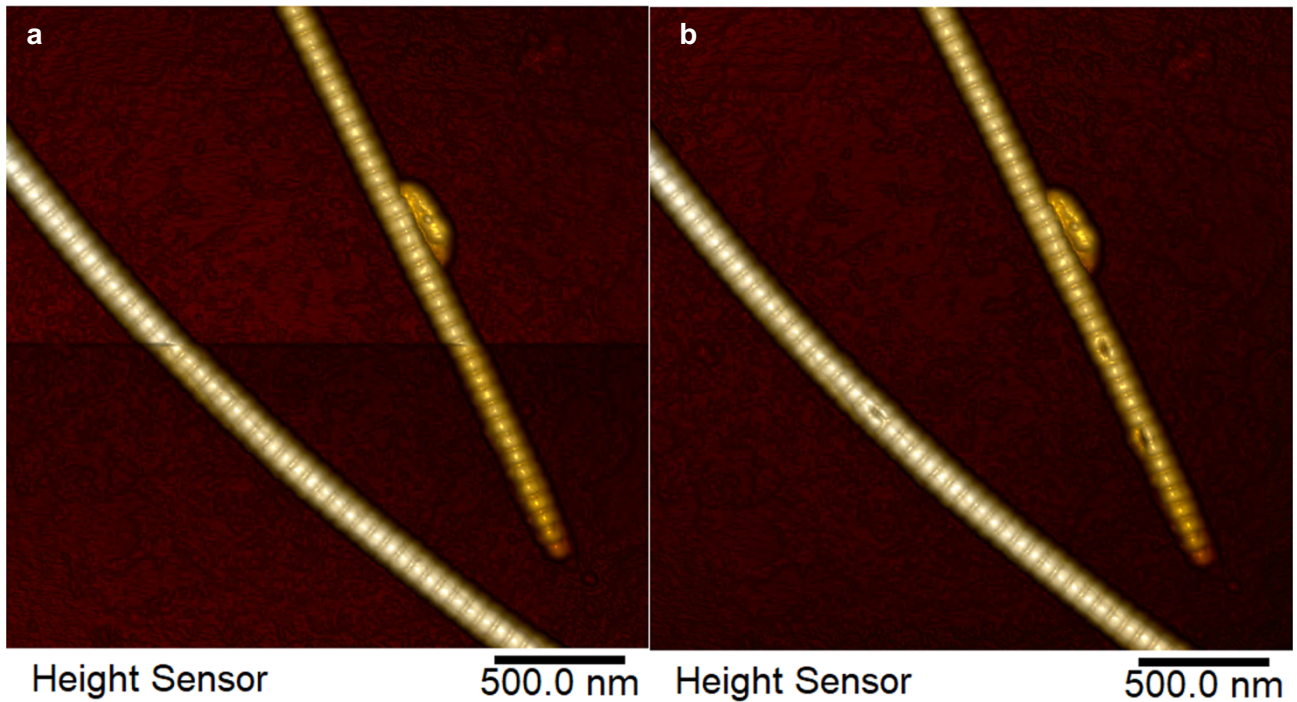
Figure 13. The presence of a discernible indentation on a collagen fibril can be observed prior to nanoindentation (a) and after the nanoindentation (b)

The Hertz model which is represented by the equation 1 below indirectly used to compute the Young's modulus from this experiment:

$$E = \frac{3\,F\,(1-v^2)}{4\,\sqrt{R}\,\delta^{\frac{3}{2}}} \qquad\qquad (1)$$

E (Elasticity)   = Young's Modulus
F   = The force applied
v = The Poisson's ratio
R   = Radius of the tip
δ = The nanoindentation

The selection of the Hertz model was based on its simplicity and widespread acceptance as a suitable representation of the mechanical behaviour of biological materials as long as the indentation remains within the elastic range of the material's reaction. Additionally, this model is widely employed for investigations pertaining to collagen fibril research. The validity of the model is dependent upon the fulfilment of the following assumptions:

1) The indenter possesses a much higher level of hardness compared to the sample, with a paraboloid shape. Different models exist for spherical, conical, and pyramidal tip forms. Nevertheless, the disparities between these models are inconsequential when the indentation is significantly smaller than the tip radius and remains within the elastic range (Mahaffy et al., 2000; Radmacher, 2002). The maximum depth of indentation in conventional nanoindentation is determined by the thickness of the sample. According to Bueckle's rule which is commonly employed in this technique, the indentation depth should be maintained at a value that is less than or equal to 10% of the sample's thickness (Bückle, 1973). This precaution is taken to prevent any potential impact from the underlying rigid substrate. There is a lack of established recommendations about the maximum depth of indentation that should not be surpassed in order to mitigate substrate impacts. The experimental findings presented in the study conducted by (Andriotis et al., 2014) indicate that in order to prevent substrate effects, it is advisable to limit the permitted depth of the indentation on collagen fibrils to a value below 10-15% of the fibril's height. In this study, the indentation depth was implemented at a level equivalent to about 3% of the height of the fibril or within the range of 0.5-1 nm, depending on the specific height of the fibril under observation. This indentation depth was chosen to ensure that the fibril remained within the elastic range throughout the experiment.

2) The specimen is characterised as a completely elastic, uniform, and isotropic solid that occupies a half-space with infinite extension (Dintwa et al., 2008; Pham, 2015).

3) Both surfaces of the specimen are smooth and devoid of friction, and there are no supplementary interactions between the indenter and the specimen (Dintwa et al., 2008; Pham, 2015).

3.4. Data Analysis

3.4.1. D-period spacing

The axial D-periodic spacing, also known as D banding, refers to the measurement of the distance between consecutive dark and light bands that are found in the collagen fibril. This spacing corresponds to the repetitive structural unit within the fibril and is utilised for the analysis of its overall structure. The measurement of D banding can be conducted using the NanoScope software by manually drawing a line across the scanned collagen fibril as shown in the figure 14.
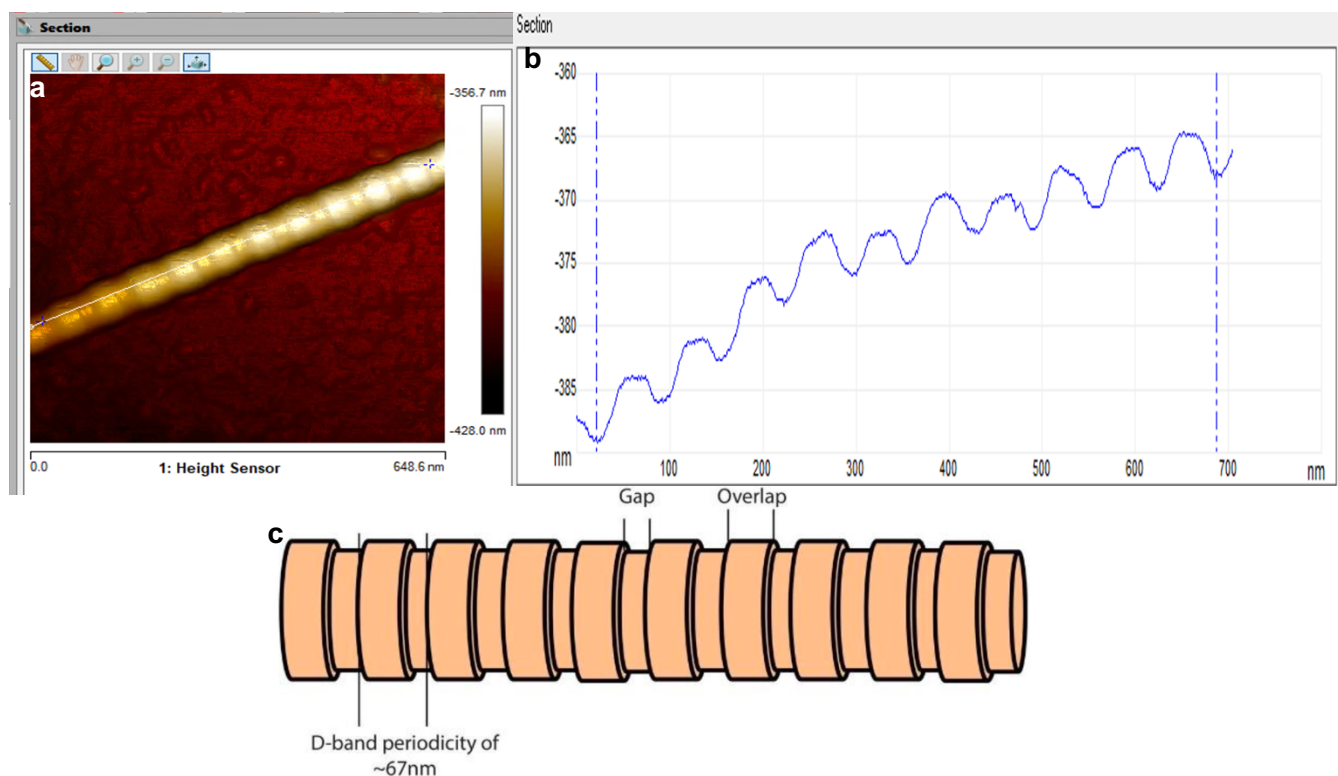
Figure 14. Determining the D-banding of the individual collagen fibril using NanoScope Analysis dissection tool (a) with the pattern of the gap and overlapping regions captured in this study (b). The detail visualisation shown in the figure (c) (Kontomaris et al., 2022)

3.4.2. Depth and Width

The dimensions of the fibrils were quantified by employing the dissection tool within the NanoScope Software. This tool facilitated the measurement of the displacement between two-user specified positions. The depth or height can be defined as the disparity between the mica (designated reference point) and the fibril. In order to determine the height of the fibril, it is necessary to choose a representative point on either the fibril itself or the surface of mica. The width refers to the measurement of the distance between the locations located on opposite sides of the fibril. In order to determine the width of the fibril, it is necessary to

select a cross-sectional area of the fibril at a specific point of interest. The measurement of depth or height is indicated by the vertical distance that lies between the blue markers, while the measurement of width is represented by the horizontal distance that lies between the red markers can be seen in the figure 15.
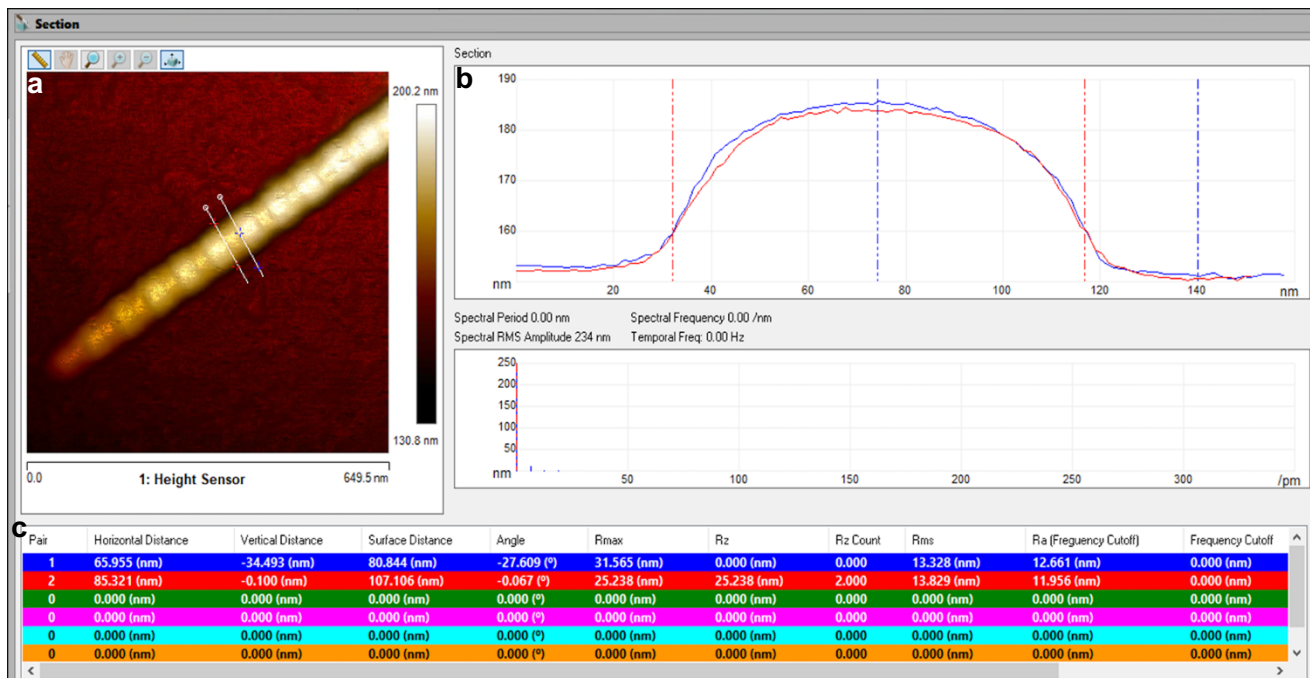
Figure 15. The thickness and width of the fibril (a) were determined using the NanoScope dissection tool (b). The thickness (represented by the vertical distance between the blue markers) was measured to be 34.5 nm. Similarly, the width (indicated by the horizontal distance between the red markers) was found to be 85.3 nm (c)

3.4.3. Young's Modulus from Nanoindentation

The Young's modulus was determined by substituting the nanoindentation value into Equation 1 of the Hertz model in conjunction with the applied force on the cantilever (20 nN), nominal tip radius (10 nm), and Poisson's Ratio (0.3). A representative force curve was obtained from the mica surface for use as a point of comparison. The curve obtained from the collagen surface was subsequently overlaid with the mica curve aligning the tip-surface contact point to achieve overlap. The horizontal separation between the two curves corresponds to the indentation (δ) of the collagen surface as depicted in Figure 15a. The measurement of collagen nanoindentation was determined by the horizontal separation between the curves representing the mica and collagen. In order to maintain consistency, the upper barrier for force fitting (max force fit boundary) was established at 39% of the

force, while the lower threshold (min force fit boundary) was set at 6% of the force. These boundaries are visually depicted in the picture through the placement of horizontal red lines as shown in the figure 16b. The selection of these two numbers was based on their ability to yield the most optimal Young's modulus value across all the collected data.
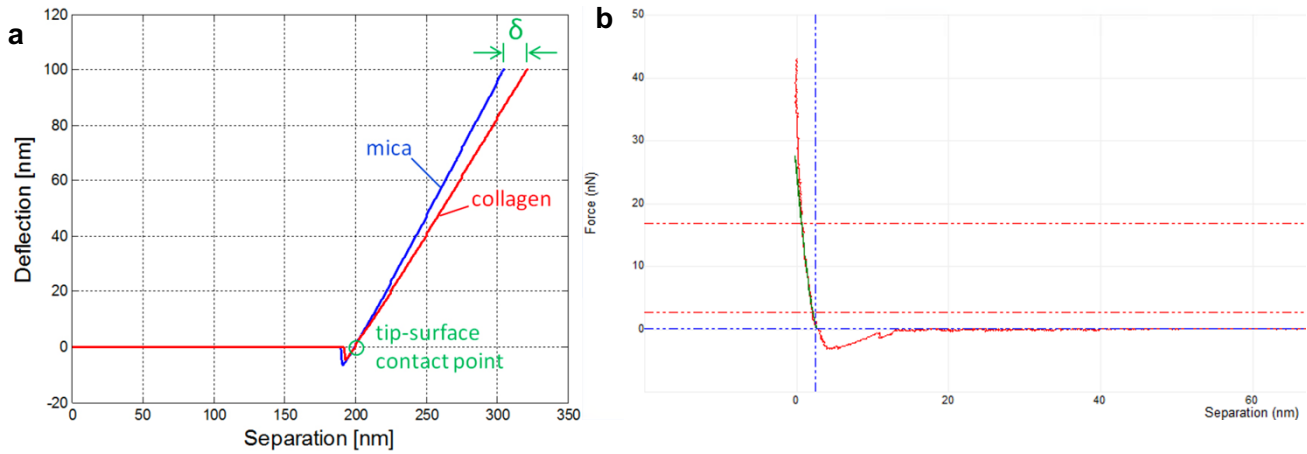
Figure 16. The presented data illustrates the relationship between tip-surface separation and tip deflection for collagen and mica surfaces (a) (Pham, 2015) and the nanoindentation force separation curve using Hertz model (b)

4. RESULTS

Expressing the author sincere gratitude to Christopher Gibson for conducting the necessary testing on the author's behalf. Given the constraints of limited time and restricted access to the AFM equipment, his contribution was crucial in obtaining the results presented in this study. This study comprised two distinct regions, each obtained from both healthy and degenerative discs (see Table 1). A total of 86 nanoindentation tests were conducted in order to get data for the mechanical test results. Due to the limited number of specimens within each data group, it was not feasible to conduct statistical analyses, such as an Analysis of Variance (ANOVA). Given that for using the ANOVA approach is based on the assumption that the data within each group follows a normal distribution and exhibits equal variances.

Considering that the sample size for each group is limited to only one (N=1), it may be inferred that the assumptions underlying the analysis would not be satisfied. Hence, the data is presented using medians and interquartile ranges (IQRs) as a result of the violation of this premise. This study involves the analysis of results obtained from graphs generated using Excel, with a focus on identifying trends. In order to ensure the validity of the test results for

subsequent data analysis, it was necessary to subject the specimen to quality control steps. These measures included verifying that the specimen had a uniform thickness of 1 mm and excluding any specimens with a Young's modulus value lower than 0.6 R^2. The coefficient of determination (R^2) is a statistical metric that offers insights into the quality of fit of a given model.

The evaluation of the goodness-of-fit between the Hertz model and experimental data in force-distance curves generated from nanoindentation commonly involves the utilisation of the R^2. A larger or the closer R^2 value to 1 signifies that the model exhibits a strong alignment with the data, whereas a smaller value implies that the model inadequately captures the observed phenomena. Hence, the selection of this number was made in order to provide improved outcomes. Upon careful examination of the collected data, it was determined that out of the total of 103 nanoindentation tests conducted, a subset of 10 tests were deemed to be inadmissible. As a result, a total of 93 tests were deemed suitable for formal analysis.

4.1. Collagen type 1 topographical imaging

The following pictures present the outcomes produced from the utilisation of the topographical imaging mode which serves to visually represent the composition of the individual collagen fibrils for ALT healthy, ALT degenerated, PST healthy and PST degenerated discs samples. The height sensor plays a vital role in the generation of topographic pictures by detecting the vertical position or height of the AFM tip throughout its scanning process across the surface of the sample. The colour scale bar is utilised to visually depict the range of values for a particular parameter observed over the scanned surface. The various colours present on the scale bar are indicative of distinct scales of the measured variable as shown in the figure 17. The darker colours correspond to the layer of mica, whilst the brighter colours correspond to the layer of fibrils.
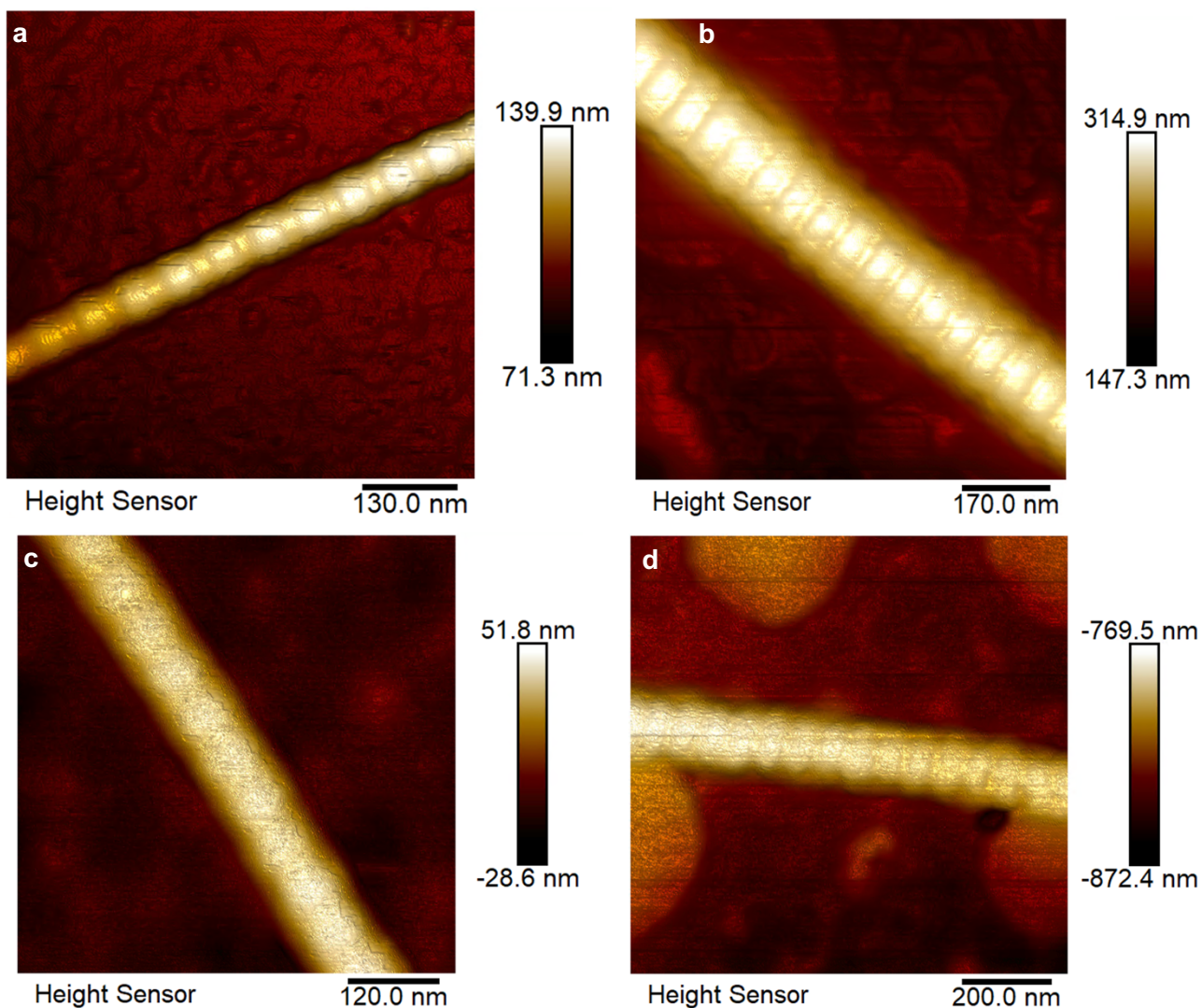
Figure 17. The visualisation of the individual collagen fibril from topographical imaging mode for ALT grade 2 (a), ALT grade 4 (b), PST grade 2 (c), and PST grade 4 (d)

The following data in table 2 presents the values corresponding to the D banding the repetitive structural unit within the fibril of the individual collagen fibrils with the sample number described where the samples were extracted from.

Table 2. The D period spacing on each region of the collagen fibril

Region	Grade	Sample Number	D banding (nm)
ALT	2	GL191447	66.7
ALT	4	GL471	67.6

PST	2	GL191447	68.3
PST	4	GL471	67.3

The provided data in table 3 displays the values associated with the sizes specifically the width and depth of the individual collagen fibrils with the size measurement was explained in chapter 3.

Table 3. The size of the individual fibrils

Region	Sample Number	Grade	Fibril	Number of Indentation	Width (nm)	Depth (nm)	Scan Size (nm)	Scan Rate (Hz)
ALT	GL191447	2	1	21	82.79	35.31	649	2
ALT	GL191447	2	2	7	85.32	34.49	650	0.602
ALT	GL191447	2	3	7	76	22.7	864	0.99
Median (IQR)					**82.79 (4.66)**	**34.49 (6.3)**	650	0.99
ALT	GL471	4	1	10	232.12	73.43	839	1.19
ALT	GL471	4	2	14	239	78.57	1660	1.19
ALT	GL471	4	3	14	243	79.44	5000	0.99
Median (IQR)					**239 (5.44)**	**78.57 (3)**	1660	1.19
PST	GL191447	2	1	13	119.54	44.16	584	1.26
PST	GL471	4	1	17	178.29	51.15	1000	1.26

4.2. Collagen type 1 Young's modulus

The tabulation of the median values for Young's modulus can be seen in Table 4. The utilisation of standard deviation as a measure of error in this particular scenario was deemed inadequate due to the limited sample size of one for each location. Furthermore, the exclusion of certain specimen data further compromised the suitability of this measure. Therefore, the median was computed for each dataset, and the IQR was graphed using Microsoft Excel. The observed disparities between the degenerated and healthy sets of samples are depicted in Figure 18.

The calculation of the IQR provides a reliable measure of the dispersion or spread exhibited by the dataset. Error bars were incorporated into the bar graphs in order to ascertain the fluctuations linked to the data points. The usage of the IQR is advantageous due to its ability to mitigate the influence of outliers present in certain data sets. Furthermore, the acquired data is non-parametric or does not adhere to a normal distribution. The IQR values for both healthy and degenerated discs are presented in Table 4 for each individual fibril and for overall can be seen in Table 5.

The PST degenerated grade 4 exhibiting a significant amount of noise that was not observed in the other datasets. Consequently, it was necessary to apply the boxcar filter tool in order to clean the data. In order to maintain consistency with the remaining data, the researcher employed the boxcar filter on all the data sets resulting in improved R^2 values for the final results. The specific information referring to this data can be observed in the appendix.

Table 4. The median Young's Modulus value on each individual fibril

Region / Grade	Fibril	Number of Indentation	Median Young's Modulus	IQR
ALT / 2	1	19	2.43 GPa	1.29
ALT / 2	2	7	1.85 GPa	0.19
ALT / 2	3	6	1.53 GPa	0.14
ALT / 4	1	10	2.7 GPa	1.18
ALT / 4	2	13	1.3 GPa	0.21
ALT / 4	3	14	2.3 GPa	3.43
PST / 2	1	11	1.13 GPa	0.16
PST / 4	1	14	3.12 GPa	0.58

Table 5. The Young's Modulus values on each region of the fibril

Region	Grade	Median Young's Modulus (GPa)	IQR	Mean Young's Modulus (GPa)	SD
ALT	2	1.91	0.84	2.49	1.67
ALT	4	2.12	1.65	2.75	2.05
PST	2	1.13	0.16	1.42	0.89
PST	4	3.12	0.58	2.88	0.69
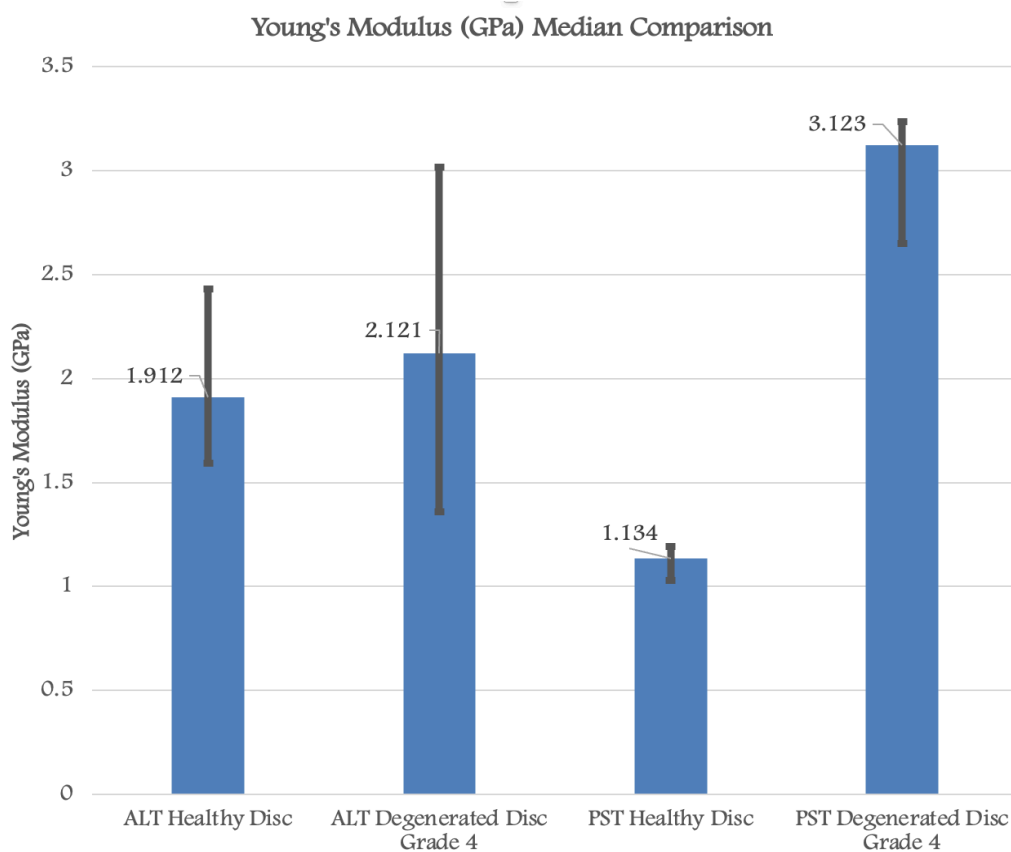
Figure 18. The median comparison values of Young's modulus along with the interquartile range between healthy and degenerative intervertebral discs for ALT and PST regions.

5. DISCUSSION

The modified technique employed in this study as developed from Dr. Pham (2015) demonstrated significant efficacy in extracting fibrils from collagen fibres with the Annulus Fibrosus (AF) tissue. The presence of individual fibrils was observable at the edges of the fibre and the process of isolating specific fibrils was not difficult. Research findings have demonstrated that the predominant collagen type within the outer AF is collagen type I as indicated by previous studies (Adams et al., 1977; Pham, 2015). Therefore, it was theorised that the fibrils present on the margins of the fibre belonged to type I. The specimens could also be distinguished based on their distinctive 67 mm D-banding pattern which was observable in the AFM pictures. Nevertheless, the efficacy of this approach may be limited when applied to gel-like substances such as the NP, since their structural integrity makes them challenging to separate (Pham, 2015).

It is important to note that the study involved a single sample size for each group of samples. The tests were conducted on one sample of ALT grade 2 (healthy) on three distinct individual collagen fibrils. Similarly, tests were conducted on one sample of ALT grade 4 (degenerated) on three different individual collagen fibrils. In the context of the PST grade 2 and 4 samples, experiments were conducted on a single fibril from each grade sample due to the limited time. Across all of the findings, there were discernible trend evident in the data collected. Nevertheless, several observations did not align with the initial hypothesis necessitating the need for a further investigation of the possible reasons in order to gain insight into the unexpected results. This chapter provides the discussion for all the results.

5.1. Collagen type 1 D banding

The banded shape is the remarkable characteristic of collagen type I fibrils (Minary-Jolandan & Yu, 2009; Wenger et al., 2007). One noticeable and intriguing feature of collagen fibres is to the arrangement of collagen molecules in a quarter-staggered configuration resulting in the formation of the D-band periodicity. This periodicity exhibits as a recurring banding pattern, around 67 nm in length, with slight variations observed across different tissues (Kontomaris et al., 2022). The individual isolated collagen fibrils can be identified by observing the characteristic D-banding or D-periodicity. The corresponding values can be found in Table 2. This identification process can be carried out by contact or intermittent contact mode imaging of AFM in the air-dried state. For visual reference, the images can be seen in Figure 17. Based on the obtained data, it is evident that there is minimal variation in

the D-band values across all samples of ALT grade 2 and 4 and also PST grade 2 and 4. The D-banding values observed in this study are within the published range of 66-68 nm, which aligns with the findings of Erickson et al. (2013). According to their research, collagen type I molecules exhibit a D-periodicity spanning from 60-73 nm (Erickson et al., 2013).

5.2. Collagen type 1 size

Table 3 shows the presence of size heterogeneity among the scanned collage fibrils even within the same sample. In the case of ALT grade 2 (healthy), the median width measures 82.79 (4.66) nm, whereas the median depth is seen to be half of that value specifically 34.49 (6.3) nm. In ALT grade 4 (degenerated), the median width measures approximately 239 (5.44) nm, while the median depth is approximately 78.57 (3) nm which is roughly double the depth of ALT grade 2 (healthy). Additionally, in the context of the PST grade 2 (healthy), the median width measures 119.54 nm, whereas the median depth is observed to be smaller at 44.16 nm. In the case of PST grade 4 (degenerated), the median width is around 178.29 nm, while the median depth is approximately 119.54 nm which is roughly twice the size observed in ALT grade 2 (healthy). The present finding is consistent with the result reported in Dr. Pham's thesis (2015) which shows that the width of the fibril approximately twice or much larger than the depth. The widths of the healthy and degenerate fibrils were measured to be 213.3±52.8 nm and 203.1±46.9 nm, respectively as reported. Furthermore, the thickness of the degenerate fibrils was 65.3±20.0 nm and the healthy fibrils measured 70.4±20.9 nm (Pham, 2015).

The diameter of the fibrils seen in this present study aligns with the findings reported by (Yang et al., 2007) which indicate that collagen possesses a hierarchical self-assembled structure characterised by fibrils ranging from 10 to 500 nm in diameter. Collagen fibrils imaged by AFM are semicylindrical, according to research conducted by (YAMAMOTO et al., 1997); this is because the scanning process initiates at the side of the tip that makes initial contact with the collagen fibril, and the tip follows a conical trajectory. Thus, the diameters of the fibrils were determined by their height rather than their width. Yamamoto (1997) examined 35 collagen fibrils of the sclera and cornea, the width and height of which varied from 80 to 550 nm (222 ± 118 nm) and 15 to 210 nm (74.2 ± 55.7 nm), respectively. The variability in fibril sizes is influenced by both the kind of tissue and age (Fratzl, 2008). Additionally, Fratzl et al. (2008) study revealed that fibril-forming collagens exhibit an average length of 300 nm and a width of around 1 nm. However, these regular structures give rise to fibrillar structures with varying lengths and diameters, which are influenced by

the anatomical position. The extensive dispersion of fibrillar structures can potentially be attributed to the composite character of several fibrils at the macro-molecular level.

According to (Parry et al., 1978), the diameters of fibrils exhibit an increase as tissue matures but undergo degradation during senescence. There are several potential factors that may account for the observed variation in fibril size within the given samples. The most possible factor is that the scanned fibrils were obtained from regions containing both thinner and thicker fibrils resulting in a range of diameters. Specifically, it is apparent that the thicker fibrils had a larger diameter in comparison to the thinner fibrils. This finding is supported by (Svensson et al., 1999) investigation which revealed that the presence of larger fibrils with diameters ranging from 150 to 250 nm compared to the thinner fibrils with diameters measuring from 50 to 80 nm.

It is required to provide clarification that collagen fibrils do not exhibit the characteristics of linear elastic solids (Kontomaris et al., 2022). Since the collagen fibril is known to consist of an alternating gap and overlapping sections with a highly consistent D-band periodicity of approximately 67 nm, the width of each fibril actually varies along the axial direction (Kontomaris et al., 2015; Minary-Jolandan & Yu, 2009). The study conducted by Liang et. al. (2017) utilised Sprague-Dawley rats as experimental subjects. The findings revealed a considerable increase in the diameters of the fibrils within the outer layer of the AF in comparison to the inner layer, observed on both the concave and convex sides (Liang et al., 2017).

Research findings have demonstrated that the diameter of fibrils does not have a significant impact on the measured mechanical properties (Andriotis et al., 2014; Wenger et al., 2007) which aligns with the results obtained. Despite the fact that the diameter of the ALT grade 4 (degenerated) is larger than that of the PST grade 4 (degenerated) as indicated in table 3, it is evident from tables 4 and 5 that the Young's modulus of the PST grade 4 (degenerated) is greater than that of the ALT grade 4 (degenerated). Moreover, despite the fact that the diameter of PST grade 2 (healthy) is larger than that of ALT grade 2 (healthy) as indicated in table 3, it is evident from tables 4 and 5 that the young's modulus of PST grade 2 (healthy) is lower than that of ALT grade 2 (healthy).

5.3. Collagen type 1 Young's modulus

To validate the methodology employed in this research, comparative analysis was conducted between the findings of this study and those of Dr. Pham's study. Specifically, the focus is on the comparison of results regarding ALT healthy and degenerated samples within the 2.5 GPa range. It is observed that the degenerated samples from Dr. Pham's study effectively exhibited the same values with the healthy samples which aligns with the results obtained in this study as shown by the data presented in Table 5. The findings of this study indicate that the mean Young's modulus of ALT grade 2 (healthy) is not statistically different to that of ALT grade 4 (degenerated). Specifically, the mean Young's modulus values for ALT grade 2 and ALT grade 4 are 2.49 GPa and 2.75 GPa, respectively as shown in the figure 19. The previously mentioned observation is further supported by a study conducted by (O'Connell et al., 2009) which involved the mechanical testing of samples orientated in the circumferential, axial, and radial directions of both degenerate and nondegenerate human AF tissues. In the case of samples orientated in the radial direction, it was observed that the toe-region modulus exhibited a stiffness that was twice as high in the presence of degeneration. Nevertheless, no additional disparities in the examined mechanical parameters were observed in degenerated samples.

30
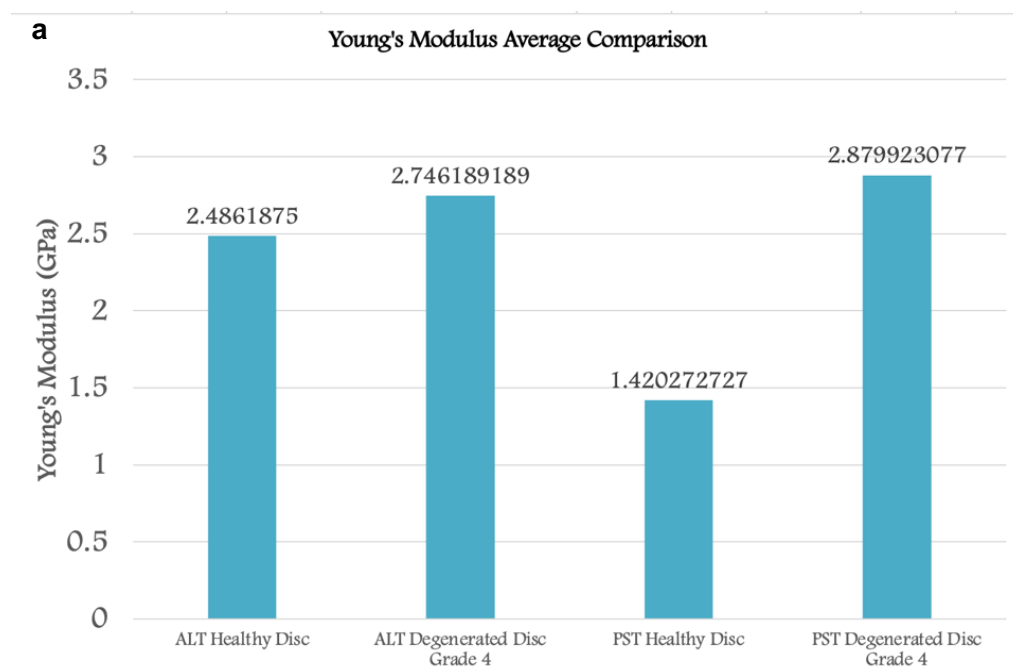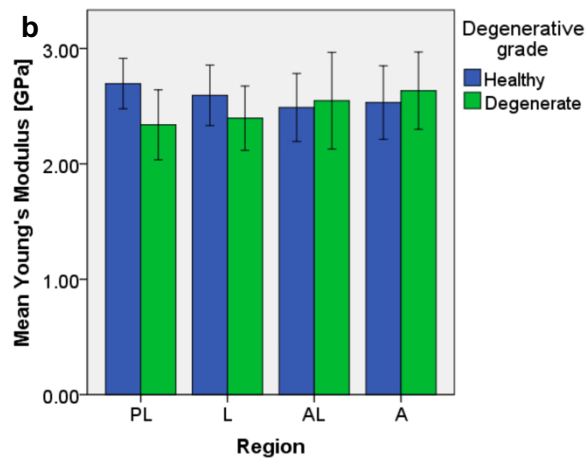
Figure 19. The mean Young's Modulus in healthy and degenerate ALT collagen fibrils from this study (a) and from Dr Pham's study in healthy and degenerate AL region (b) (Pham, 2015) observed no statistically significant variations from both findings.

The variability of the Young's modulus values for individual collagen fibrils is demonstrated by the findings presented in Chapter 4. The variability in the values of Young's modulus, even within the same sample, is depicted in Table 4. Regarding the ALT grade 2 and grade 4 samples, three distinctive fibrils from a single sample for each grade during the testing process. In contrast, for the PST samples of grades 2 and 4, we conducted testing exclusively on a single fibril for each grade. According to the data presented in Table 5, it can be observed that the median (IQR) young's modulus for ALT grade 2 is 1.91 (0.84) GPa, which is lower than that of ALT grade 4, which is 2.12 (1.65) GPa. This suggests that the difference in young's modulus between these two grade levels is negligible. The median Young's modulus for grade 2 PST is clearly 1.13 (0.16) GPa which is the smallest value observed among the other samples. On the contrary, the median Young's modulus of grade 4 PST is 3.12 (0.58) GPa which is greater than the values found in the remaining samples. This finding showed that the PST region has a substantial degenerative impact when compared to the ALT region based on the trend. However, it is important to note that the findings of this study cannot be considered optimal due to the limited sample size of only one.

Research done by Zhou et al. (2023) found that herniations frequently occur in the posterolateral or posterior region of the IVD. Protrusion, extrusion, or sequestration are the three classifications applicable to these herniations, contingent upon the degree of tissue continuity present within the disc space. In the 1990s, an analysis of healthy and degenerated tissue revealed that relative to the anterior AF, the thickness of the posterior and posterolateral AF decreased by 15% to 25% and the number of incomplete lamellae increased by 25% to 80% (Marchand & Ahmed, 1990; Tsuji et al., 1993). These variations

31

are likely responsible for the decreased sub-failure and failure qualities in the posterior AF; thus, the posterior and posterolateral AF are identified as intrinsic areas of vulnerability for disc failure (Acaroglu et al., 1995; Ebara et al., 1996; Zhou et al., 2023). The observation is consistent with the findings that the young's modulus of PST grade 2 (healthy) is relatively less than both grade 2 (healthy) and grade 4 (degenerated) ALT.

The increased Young's modulus observed in the degraded grade 4 PST trend in this investigation could be attributed to a number of probable factors including the dehydration state of the fibril (Andriotis et al., 2014), inaccuracies in the processing of data (Kontomaris & Malamou, 2020), and uncertainties pertaining to the calibration protocols of the AFM probe (Wenger et al., 2007). According to Kontomaris et. al (2022), in addition to considering the water concentration within the fibril, it is important to acknowledge that the range of Young's modulus values obtained for dry collagen fibrils is remarkably wide even when employing identical experimental conditions which is corresponding to the findings in the results section chapter 4. This observation is consistent with the water concentration within the fibril. The Young's modulus values for individual dry collagen fibrils derived from a variety of tissues vary between 0.9 and 11.5 GPa according to the findings of several studies (Wenger et al., 2007; Andriotis et al., 2014; Kontomaris et al., 2022; Kontomaris et al., 2015). In addition, the AFM calibration procedures comprise the precise determination of the tip's shape and size, as well as the spring constant of the AFM cantilever (Kontomaris et al., 2022; Wenger et al., 2007). However, the most probable cause is likely because of the dehydration state of the fibril.

The influence of ambient variables on the outcomes of AFM measurements conducted on biological samples has been widely acknowledged (Kontomaris et al., 2022). Specifically, the humidity levels have been observed to impact the contact between the AFM tip and the sample surface, thereby leading to modifications in the mechanical properties of the sample (Sobola et al., 2020).

In addition, the considerable variation in Young's modulus values stated in the scientific literature is primarily due to the mechanical heterogeneity of collagen which is caused by the presence of gap and overlapping regions. This heterogeneity is strongly correlated with the condition of collagen dehydration of the collagen. In the research by Spitzner et al. (2015) utilised purified type 1 collagen extracted from bovine hide to assess the influence of water on the nanoscale mechanical properties of individual type I collagen fibrils. When the fibril is hydrated, the mechanical differentiation between overlapping and gap regions

becomes significant, whereas it is negligible when the material is dried (Spitzner et al., 2015).

In this research, the samples were first created on mica and thereafter stored in a tiny container until they were ready to be examined via AFM. Prior to being evaluated under AFM, the samples were not rehydrated using phosphate-buffered saline (PBS). The nanomechanical characteristics of collagen fibrils are influenced by alterations in their hydration levels (Andriotis et al., 2018). The impact of hydration on collagen fibril mechanics has been identified as a significant contributor (Masic et al., 2015). This influence is believed to occur due to alterations in the density of noncovalent contacts, which have been directly evaluated at the collagen fibril level during tension (Andriotis et al., 2018) and indentation-type loading (Grant et al., 2008, 2009).

The utilisation of indentation-type AFM loading in the study conducted by (Andriotis et al., 2015) shown a significant disparity of three to four orders of magnitude in the indentation modulus when comparing hydrated and air-dried collagen fibrils. In addition to AFM, another testing technique known as Brillouin light scattering (BLS) has also demonstrated alterations in the observed spectra during the process of collagen dehydration (Cusack & Lees, 1984; Cusack & Miller, 1979; Harley et al., 1977). In a study conducted by (Andriotis et al., 2019), it was seen that the peak position exhibited an upward shift in both the control and ribose-treated samples as dehydration occurred. This shift in peak position was found to be indicative of an increase in the material's stiffness (Andriotis et al., 2019). This finding aligns with previous research conducted on the dehydration process of collagen fibres (Cusack & Lees, 1984; Palombo et al., 2014).

The indentation modulus of collagen fibrils that have been air-dried falls within the range of 1-10 GPa, as reported in previous studies (Andriotis et al., 2015; Andriotis et al., 2014; Grant et al., 2008; Heim et al., 2006; Wenger et al., 2007). The packing density of collagen fibrils falls significantly with hydration, resulting in a large decrease in the indentation modulus by approximately three orders of magnitude (Andriotis et al., 2019). Hence, these factors could potentially account for the unexpectedly elevated values of median Young's modulus seen in the single PST grade 4 (degenerated) sample. This is due to the direct correlation between the duration of samples dehydrated and the subsequent increase in Young's modulus.

Based on the findings of this research, it can be observed that there is a discernible trend of degeneration affecting the Young's modulus value, particularly in the posterior region. However, it is important to note that the small sample size limits the robustness of the

inferences drawn. Additionally, it is worth considering that the high Young's modulus value may be influenced by the role of dehydration in this context. In addition to the existing literature and corresponds to the finding by the previous study by (Pham, 2015), it has been observed that degeneration does not specifically target collagen type I, but rather may have a more significant effect on the nucleus pulposus (NP). Moreover, considering the observed variations in patterns, it is probable that the alteration in the mechanical properties of the AF in distinct anatomical regions of the IVD is mostly attributed to a modification in the organisation of collagen fibrils, rather than an intrinsic transformation of the fibre bundles and fibrils themselves. It is possible that degenerative disc disease does not specifically affect the proteins involved in the synthesis of collagen fibrils.

5.4. Limitations

The primary objective of the study was to compare the stiffness of collagen type 1 between healthy and degenerative discs. The investigation was effectively conducted; however several limitations were encountered. The limited sample size of one participant in each group (healthy and degenerated disc) for the ALT and PST regions precluded the possibility of doing a statistical analysis on the data. Furthermore, certain tested points of data were unable to be included in the formal results. Significant variability was observed in certain data sets due to the limited availability of a single specimen per data group for testing using the AFM machine. Hence, the limits of comparing the acquired results with those of other studies were evident.

The acquisition of human IVD specimens posed challenges due to their limited availability. Consequently, thorough precautions were implemented to maintain the quality of the specimens during their preparation and handling procedures. As a result of this researcher's constrained timeline and limited access to the AFM machine at the Bedford Park campus, they were unable to personally conduct the testing of the prepared samples. Consequently, they received assistance from the AFM lab coordinator who performed the testing.

The tests necessitate a significant amount of time for both data collection and analysis, which restricts the acquisition of a large number of datasets necessary for reliable data interpretation. Furthermore, it would be beneficial to utilise alternative models of AFM nanoindentation in order to get further understanding and differentiate the outcomes obtained from each model. Moreover, the diversity in the morphology and surface texture of the nanoindenter's tip could potentially result in an irregular distribution of the recorded data.

Throughout the initial stages of the experiment, the adjustment of the screw mechanism in the microtome proved to be challenging and necessitated servicing throughout the practise phase. This guaranteed that the system performed effectively during both the pilot and formal testing phases.

The hydration condition of the specimen may have been influenced by the freeze-thawing cycles it underwent. It is important to consider that the examination of mechanical properties of the IVD samples is more effectively conducted by doing comparisons under identical freeze/thaw cycles, as suggested by (Azarnoosh et al., 2017). It may be advantageous to do testing on a consistent set of specimens that have undergone an equal number of thawing and freezing cycles.

6. POSSIBLE FUTURE WORK

As previously stated, the short timeframe resulted in insufficient sample sizes for doing statistical analysis. Consequently, it would be advantageous to employ statistical methods, such as analysis of variance (ANOVA), to evaluate the data in this study. Regarding the processing of the samples, it is noteworthy that the nanoindentations in these studies were not conducted immediately upon hydration. However, it was feasible to examine the samples under hydrated conditions or rehydrate them using phosphate-buffered saline (PBS).

 It is advisable to conduct the nanoindentations in circumstances that closely simulate the physiological environment for optimal results. In addition, this work employed a mica substrate as the experimental foundation. It would be advantageous to observe the samples utilising alternative substrates, such as silicon, in order to have a comprehensive understanding of the influence of the substrate on data acquisition. Multiple studies have demonstrated that the comparison between dry and hydrated settings suggests that conducting tests in a fluid environment will likely result in reduced Young's Modulus values.

Considering the limited existing study on the IVD of the AF particularly in relation to the posterior region, it would be beneficial to conduct comprehensive investigations involving both circumferential and radial dimensions of the PST region. While AFM nanoindentation is widely employed and recognised as a standard method for studying the mechanical characteristics of collagen fibrils, direct tensile testing would be preferable due to its potential to modify strain rate by adjusting the speed of tip approach and retract modes. Furthermore,

it is necessary for future investigations to elucidate the potential alterations in the nanomechanical properties of the NP degenerated in relation to the depth of indentation, the direction of testing, and the moisture content. These experiments are expected to provide more understanding of the nanomechanical properties of the NP and contribute to the use of AFM techniques in practical treatments.

7. CONCLUSION

The approach employed in this study was deemed reliable and robust offering potential for further investigation into the nanomechanical properties of collagen type 1 in the annulus fibrosus (AF) of human intervertebral discs. The primary objective of this study was to conduct a comparative analysis of the nanomechanical characteristics of human collagen type 1, specifically examining healthy and degenerated samples obtained from the AF. To accomplish this objective, the atomic force microscopy (AFM) nanoindentation technique was employed to generate force-displacement data. Subsequently, the obtained data was utilised to calculate the Young's modulus using the Hertz Model. This analysis was performed in two distinct regions of the disc. In general, it is worth noting that there was a discernible disparity in the values of the young's modulus between the degenerated and healthy specimens in the PST region. The wide range of Young's modulus values observed in collagen fibrils can be attributed to their inherent structural and mechanical variability. The Young's modulus values pertaining to collagen fibrils remain unaltered in the presence of disc degeneration. This information may offer elucidation on the specific protein types impacted by degenerative disc disease, as well as identify the specific regions within the disc that necessitate focused attention for the development of prospective remedies. The utilisation of AFM for nanoindentation encounters some constraints when applied to biological tissue.

BIBLIOGRAPHY

Australian Institute of Health and Welfare. (2023). Back problems. Retrieved from

https://www.aihw.gov.au/reports/chronic-musculoskeletal-conditions/back-problems.

  Accessed October 2023.

Adams, M. A. (2015). Intervertebral Disc Tissues. In B. Derby & R. Akhtar (Eds.), *Mechanical Properties of Aging Soft Tissues* (pp. 7-35). Springer International Publishing. https://doi.org/10.1007/978-3-319-03970-1_2

Adams, P., Eyre, D., & Muir, H. (1977). Biochemical aspects of development and ageing of human lumbar intervertebral discs. *Rheumatology, 16*(1), 22-29.

Andriotis, O., Chang, S., Vanleene, M., Howarth, P., Davies, D., Shefelbine, S., Buehler, M., & Thurner, P. (2015). Structure–mechanics relationships of collagen fibrils in the osteogenesis imperfecta mouse model. *Journal of the Royal Society Interface, 12*(111), 20150701.

Andriotis, O. G., Desissaire, S., & Thurner, P. J. (2018). Collagen fibrils: Nature's highly tunable nonlinear springs. *ACS nano, 12*(4), 3671-3680.

Andriotis, O. G., Elsayad, K., Smart, D. E., Nalbach, M., Davies, D. E., & Thurner, P. J. (2019). Hydration and nanomechanical changes in collagen fibrils bearing advanced glycation end-products. *Biomedical optics express, 10*(4), 1841-1855.

Andriotis, O. G., Manuyakorn, W., Zekonyte, J., Katsamenis, O. L., Fabri, S., Howarth, P. H., Davies, D. E., & Thurner, P. J. (2014). Nanomechanical assessment of human and murine collagen fibrils via atomic force microscopy cantilever-based nanoindentation. *Journal of the Mechanical Behavior of Biomedical Materials, 39*, 9-26. https://doi.org/https://doi.org/10.1016/j.jmbbm.2014.06.015

Azarnoosh, M., Stoffel, M., Quack, V., Betsch, M., Rath, B., Tingart, M., & Markert, B. (2017). A comparative study of mechanical properties of fresh and frozen-thawed porcine intervertebral discs in a bioreactor environment. *Journal of the Mechanical Behavior of Biomedical Materials, 69*, 169-177.

Balasubramanian, P., Prabhakaran, M. P., Sireesha, M., & Ramakrishna, S. (2013). Collagen in Human Tissues: Structure, Function, and Biomedical Implications from a Tissue Engineering Perspective. In A. Abe, H.-H. Kausch, M. Möller, & H. Pasch (Eds.), *Polymer Composites – Polyolefin Fractionation – Polymeric Peptidomimetics – Collagens* (pp. 173-206). Springer Berlin Heidelberg. https://doi.org/10.1007/12_2012_176

Bogduk, N. (2005). *Clinical anatomy of the lumbar spine and sacrum*. Elsevier Health Sciences.

Bückle, H. (1973). Use of the hardness test to determine other material properties. *The science of hardness testing and its research applications, 453*.

Buckwalter, J. A. (1995). Aging and degeneration of the human intervertebral disc. *Spine, 20*(11), 1307-1314.

Butt, H.-J., Cappella, B., & Kappl, M. (2005). Force measurements with the atomic force microscope: Technique, interpretation and applications. *Surface science reports, 59*(1-6), 1-152.

Cappella, B., & Dietler, G. (1999). Force-distance curves by atomic force microscopy. *Surface science reports, 34*(1-3), 1-104.

Cassidy, J., Hiltner, A., & Baer, E. (1989). Hierarchical structure of the intervertebral disc. *Connective tissue research, 23*(1), 75-88.

Cortes, D. H., & Elliott, D. M. (2014). The Intervertebral Disc: Overview of Disc Mechanics. In I. M. Shapiro & M. V. Risbud (Eds.), *The Intervertebral Disc: Molecular and Structural Studies of the Disc in Health and Disease* (pp. 17-31). Springer Vienna. https://doi.org/10.1007/978-3-7091-1535-0_2

Cusack, S., & Lees, S. (1984). Variation of longitudinal acoustic velocity at gigahertz frequencies with water content in rat-tail tendon fibers. *Biopolymers: Original Research on Biomolecules, 23*(2), 337-351.

Cusack, S., & Miller, A. (1979). Determination of the elastic constants of collagen by Brillouin light scattering. *Journal of molecular biology, 135*(1), 39-51.

Dintwa, E., Tijskens, E., & Ramon, H. (2008). On the accuracy of the Hertz model to describe the normal contact of soft elastic spheres. *Granular Matter*, *10*(3), 209-221. https://doi.org/10.1007/s10035-007-0078-7

Eppell, S., Smith, B., Kahn, H., & Ballarini, R. (2006). Nano measurements with micro-devices: mechanical properties of hydrated collagen fibrils. *Journal of the Royal Society Interface*, *3*(6), 117-121.

Erickson, B., Fang, M., Wallace, J. M., Orr, B. G., Les, C. M., & Banaszak Holl, M. M. (2013). Nanoscale structure of type I collagen fibrils: quantitative measurement of D-spacing. *Biotechnology journal*, *8*(1), 117-126.

Feigin, V. (2016). Global, regional, and National Incidence, prevalence, and years lived with disability for 310 acute and chronic diseases and injuries, 1990-2015: a systematic analysis for the global burden of disease study 2015. *The Lancet*, *388*(10053), 1545-1602.

Filanowski, A., Sarver, J., Miller, G., Bowles, R., Soslowsky, L., & Elliott, D. (2003). Reduced type I collagen alters disc mechanical properties in genetically engineered mice. *Trans Orthop Res Soc*, *28*, 25.

Fratzl, P. (2008). Collagen: Structure and Mechanics, an Introduction. In P. Fratzl (Ed.), *Collagen: Structure and Mechanics* (pp. 1-13). Springer US. https://doi.org/10.1007/978-0-387-73906-9_1

Graham, J. S., Vomund, A. N., Phillips, C. L., & Grandbois, M. (2004). Structural changes in human type I collagen fibrils investigated by force spectroscopy. *Experimental cell research*, *299*(2), 335-342.

Grant, C. A., Brockwell, D. J., Radford, S. E., & Thomson, N. H. (2008). Effects of hydration on the mechanical response of individual collagen fibrils. *Applied Physics Letters*, *92*(23).

Grant, C. A., Brockwell, D. J., Radford, S. E., & Thomson, N. H. (2009). Tuning the elastic modulus of hydrated collagen fibrils. *Biophysical journal*, *97*(11), 2985-2992.

Gutsmann, T., Fantner, G. E., Kindt, J. H., Venturoni, M., Danielsen, S., & Hansma, P. K. (2004). Force spectroscopy of collagen fibers to investigate their mechanical properties and structural organization. *Biophysical journal*, *86*(5), 3186-3193.

Hang, F., & Barber, A. H. (2011). Nano-mechanical properties of individual mineralized collagen fibrils from bone tissue. *Journal of the Royal Society Interface*, *8*(57), 500-505.

Harley, R., James, D., Miller, A., & White, J. (1977). Phonons and the elastic moduli of collagen and muscle. *Nature*, *267*(5608), 285-287.

Heim, A. J., Matthews, W. G., & Koob, T. J. (2006). Determination of the elastic modulus of native collagen fibrils via radial indentation. *Applied Physics Letters*, *89*(18).

Hutter, J. L., & Bechhoefer, J. (1993). Calibration of atomic-force microscope tips. *Review of scientific instruments*, *64*(7), 1868-1873.

Johnson, D., Oatley-Radcliffe, D. L., & Hilal, N. (2017). Chapter 7 - Atomic Force Microscopy (AFM). In N. Hilal, A. F. Ismail, T. Matsuura, & D. Oatley-Radcliffe (Eds.), *Membrane Characterization* (pp. 115-144). Elsevier. https://doi.org/https://doi.org/10.1016/B978-0-444-63776-5.00007-3

Junqueira, L. C. U., & Carneiro, J. (2005). Basic histology: text & atlas.

Kontomaris, S. V., Stylianou, A., & Malamou, A. (2022). Atomic force microscopy nanoindentation method on collagen fibrils. *Materials*, *15*(7), 2477.

Kontomaris, S. V., Yova, D., Stylianou, A., & Balogiannis, G. (2015). The effects of UV irradiation on collagen D-band revealed by atomic force microscopy. *Scanning*, *37*(2), 101-111.

Lewis, N. T., Hussain, M. A., & Mao, J. J. (2008). Investigation of nano-mechanical properties of annulus fibrosus using atomic force microscopy. *Micron*, *39*(7), 1008-1019.

Liang, T., Zhang, L.-L., Xia, W., Yang, H.-L., & Luo, Z.-P. (2017). Individual collagen fibril thickening and stiffening of annulus fibrosus in degenerative intervertebral disc. *Spine*, *42*(19), E1104-E1111.

Lorenzo, A. C., & Caffarena, E. R. (2005). Elastic properties, Young's modulus determination and structural stability of the tropocollagen molecule: a computational study by steered molecular dynamics. *Journal of biomechanics*, *38*(7), 1527-1533.

Mahaffy, R., Shih, C., MacKintosh, F., & Käs, J. (2000). Scanning probe-based frequency-dependent microrheology of polymer gels and biological cells. *Physical review letters*, *85*(4), 880.

Masic, A., Bertinetti, L., Schuetz, R., Chang, S.-W., Metzger, T. H., Buehler, M. J., & Fratzl, P. (2015). Osmotic pressure induced tensile forces in tendon collagen. *Nature communications*, *6*(1), 5942.

Minary-Jolandan, M., & Yu, M.-F. (2009). Nanomechanical heterogeneity in the gap and overlap regions of type I collagen fibrils with implications for bone heterogeneity. *Biomacromolecules*, *10*(9), 2565-2570.

O'connell, G., Vresilovic, E., & Elliott, D. (2006). Comparative intervertebral disc anatomy across several animal species. 52nd Annual Meeting of the Orthopaedic Research Society,

O'Connell, G. D., Guerin, H. L., & Elliott, D. M. (2009). Theoretical and uniaxial experimental evaluation of human annulus fibrosus degeneration.

Osti, O., Vernon-Roberts, B., Moore, R., & Fraser, R. (1992). Annular tears and disc degeneration in the lumbar spine. A post-mortem study of 135 discs. *The Journal of Bone & Joint Surgery British Volume*, *74*(5), 678-682.

Ottani, V., Martini, D., Franchi, M., Ruggeri, A., & Raspanti, M. (2002). Hierarchical structures in fibrillar collagens. *Micron*, *33*(7-8), 587-596.

Palombo, F., Winlove, C. P., Edginton, R. S., Green, E., Stone, N., Caponi, S., Madami, M., & Fioretto, D. (2014). Biomechanics of fibrous proteins of the extracellular matrix studied by Brillouin scattering. *Journal of the Royal Society Interface*, *11*(101), 20140739.

Parry, D., Barnes, G., & Craig, A. (1978). A comparison of the size distribution of collagen fibrils in connective tissues as a function of age and a possible relation between fibril size distribution and mechanical properties. *Proceedings of the Royal Society of London. Series B. Biological Sciences*, *203*(1152), 305-321.

Pham, D. (2015). *Multiscale Mechanical Investigations of the Human Anulus Fibrosus* Flinders University, School of Computer Science, Engineering and Mathematics.].

Radmacher, M. (2002). 4.-Measuring the elastic properties of living cells by the atomic force microscope. *Methods in cell biology, 68*(1), 67-90.

Robbins, C. R. (2002). Interactions of shampoo and crème rinse ingredients with human hair. *Chemical and physical behavior of human hair*, 193-310.

Sasaki, N., & Odajima, S. (1996). Stress-strain curve and Young's modulus of a collagen molecule as determined by the X-ray diffraction technique. *Journal of biomechanics*, *29*(5), 655-658.

Schollmeier, G., Lahr-Eigen, R., & Lewandrowski, K.-U. (2000). Observations on fiber-forming collagens in the anulus fibrosus. *Spine*, *25*(21), 2736-2741.

Serry, F. (2005). Improving the accuracy of AFM force measurements: The thermal tune solution to the cantilever spring constant problem. *Veeco Application Notes*, *14*.

Shen, Z. L., Dodge, M. R., Kahn, H., Ballarini, R., & Eppell, S. J. (2008). Stress-strain experiments on individual collagen fibrils. *Biophysical journal*, *95*(8), 3956-3963.

Shen, Z. L., Kahn, H., Ballarini, R., & Eppell, S. J. (2011). Viscoelastic properties of isolated collagen fibrils. *Biophysical journal*, *100*(12), 3008-3015.

Smith, L. J., Nerurkar, N. L., Choi, K.-S., Harfe, B. D., & Elliott, D. M. (2011). Degeneration and regeneration of the intervertebral disc: lessons from development. *Disease models & mechanisms*, *4*(1), 31-41.

Strasser, S., Zink, A., Janko, M., Heckl, W. M., & Thalhammer, S. (2007). Structural investigations on native collagen type I fibrils using AFM. *Biochemical and biophysical research communications*, *354*(1), 27-32.

Stylianou, A., Kontomaris, S.-V., Grant, C., & Alexandratou, E. (2019). Atomic force microscopy on biological materials related to pathological conditions. *Scanning*, *2019*.

Svensson, L., Aszódi, A., Reinholt, F. P., Fässler, R., Heinegård, D., & Oldberg, Å. (1999). Fibromodulin-null mice have abnormal collagen fibrils, tissue organization, and altered lumican deposition in tendon. *Journal of Biological Chemistry*, *274*(14), 9636-9647.

Svensson, R. B., Hassenkam, T., Hansen, P., & Magnusson, S. P. (2010). Viscoelastic behavior of discrete human collagen fibrils. *Journal of the Mechanical Behavior of Biomedical Materials*, *3*(1), 112-115.

Thompson, R. E., Pearcy, M. J., Downing, K. J., Manthey, B. A., Parkinson, I. H., & Fazzalari, N. L. (2000). Disc lesions and the mechanics of the intervertebral joint complex. *Spine*, *25*(23), 3026-3035.

Van Der Rijt, J. A., Van Der Werf, K. O., Bennink, M. L., Dijkstra, P. J., & Feijen, J. (2006). Micromechanical testing of individual collagen fibrils. *Macromolecular bioscience*, *6*(9), 697-702.

Viidik, A. (1973). Functional properties of collagenous tissues. *International review of connective tissue research*, *6*, 127-215.

Wenger, M. P., Bozec, L., Horton, M. A., & Mesquida, P. (2007). Mechanical properties of collagen fibrils. *Biophysical journal*, *93*(4), 1255-1263.

YAMAMOTO, S., HITOMI, J., SHIGENO, M., SAWAGUCHI, S., ABE, H., & USHIKI, T. (1997). Atomic force microscopic studies of isolated collagen fibrils of the bovine cornea and sclera. *Archives of histology and cytology*, *60*(4), 371-378.

Yang, L., van der Werf, K. O., Koopman, B. F., Subramaniam, V., Bennink, M. L., Dijkstra, P. J., & Feijen, J. (2007). Micromechanical bending of single collagen fibrils using atomic force microscopy. *Journal of Biomedical Materials Research Part A*, *82*(1), 160-168.

APPENDICES

Appendix A: AFM Cantilever Stiffness Calibration

The is a highly precise equipment used for measuring forces. However, it is important to note that sensitivity and measurement accuracy are distinct matters. The purpose of this application note is to elucidate a proposed approach for enhancing the precision of AFM force measurements by means of a more meticulous calibration of the spring constant of the AFM cantilever (Serry, 2005). Identifying the cantilever spring constant is a crucial parameter requiring precise measurement for force spectroscopy.

The force sensitivity of the AFM probe is partially determined by the stiffness of the cantilever. This property is often measured using the spring constant (denoted as k). The force (F) exerted on the cantilever at the location of the tip is directly correlated to the displacement (z) of the cantilever's free end from its equilibrium position. In the context of Hooke's law, it can be said that the F acting on an object is directly proportional to the z of the object from its equilibrium position, with a proportionality constant represented by k. This description adequately characterises the true situation where the deflection of the cantilever is quite modest in comparison to its thickness, and the thickness itself is relatively small in comparison to the length of the cantilever, focusing just on the cantilever geometry (Serry, 2005).

Thermal tuning is a calibration method that is extensively employed and acknowledged by determining the stiffness of a cantilever by analysing its mechanical reaction to thermal noise (Hutter & Bechhoefer, 1993; Pham, 2015; Serry, 2005). The technique discussed here is the default calibration programme implemented in the NanoScope software. It operates on the fundamental idea that a harmonic oscillator will exhibit fluctuations in reaction to thermal noise when in a state of equilibrium with its surrounding environment. In the scenario where the cantilever is seen as a simple harmonic oscillator with a single degree of freedom (DOF), thermal noise is introduced to the cantilever system, and the resulting variations are observed over a period of time (Pham, 2015). The frequency spectrum can be deduced and subsequently fitted with a Lorentzian model in which its peak of spectrum corresponds to the resonant frequency of the cantilever. P denotes as the area under the curve, denoted as P, serves as an indicator of the magnitude of the fluctuations' power. The k can be determined by employing Equation (2) which incorporates the constant of Boltzmann (kB)

and the temperature (T), with the latter being assumed to be 21∘C. The resonant frequency of the cantilever is denoted by the peak of the curve as shown in the figure 20.

$$k = \frac{k_B\,T}{P} \qquad\qquad (2)$$

k   = Spring constant of the cantilever

k_B = The constant of Boltzmann

T = Temperature

P   = Area under the curve
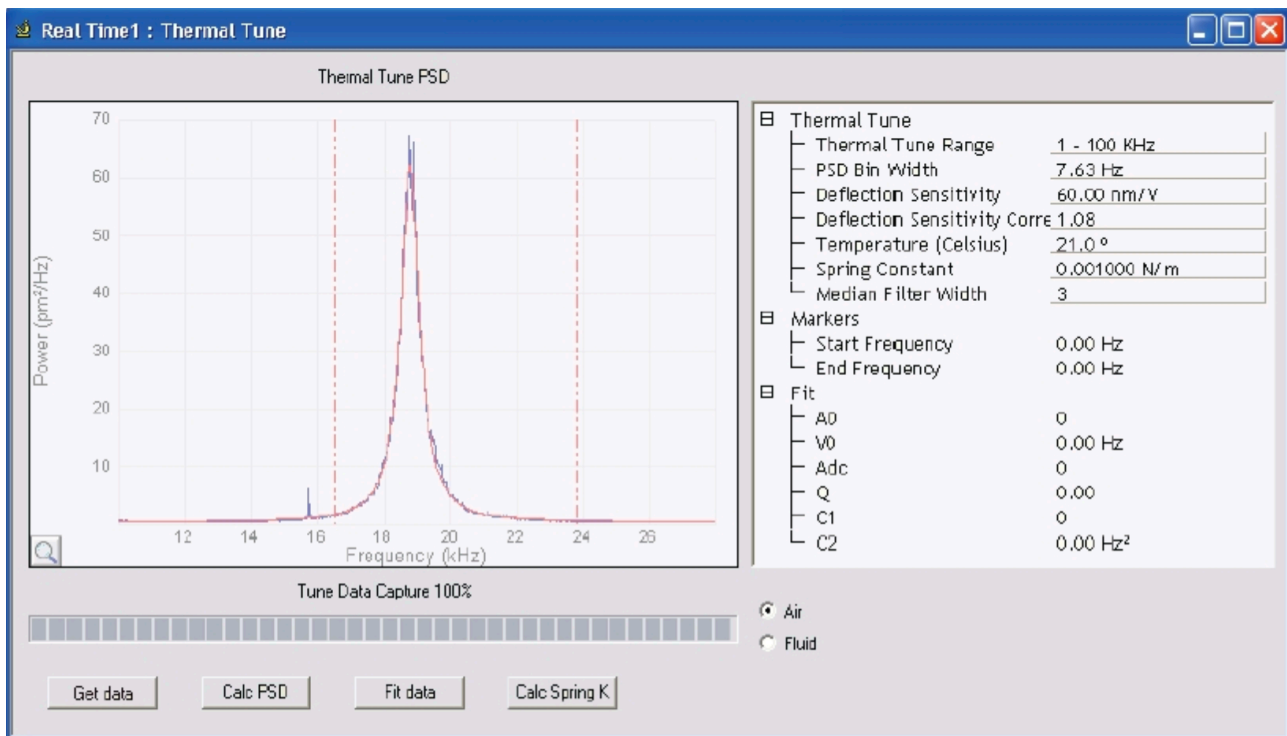
Figure 20. The illustration of thermal tuning data with the blue plot depicts power spectral density and red plot shows a Lorentzian curve (Serry, 2005).

Appendix B: Tip Specification

The AFM tests done utilising Bruker FMV probe, it is rectangular in geometry and made by antimony (n) doped silicon which are capable of operating in both contact and tapping modes. This Bruker's value line probe is suitable for gentle tapping mode and force modulation particularly when handling delicate samples. It possesses nominal spring constants ranging from 1 N/m to 5 N/m, with a specific value of 2.8 N/m (Bruker, 2013). The spring constants for all tips utilised in this study have been determined and are presented in figure 21. A total of 4 tips were employed to carry out the four AFM investigations which involved one disc each for two distinct regions for both healthy and degenerated. Thermal

tuning proved to be a precise technique in the calibration of AFM tips employed in nanoindentation, as it yielded spring constant values (Pham, 2015; Serry, 2005).

Region	Sample Number	Grade	Fibril	Spring Constant (N/m)	Tip
ALT	GL191447	2	1	1.95	1
			2	1.95	1
			3	1.95	1
ALT	GL471	4	1	1.95	1
			2	2.46	2
			3	2.46	2
PST	GL191447	2	1	2.46	3
PST	GL471	4	1	2.46	4

Figure 21. Constants of spring cantilevers for four FMV tips employed in nanoindentation

Appendix C: Sensitivity Calculation

The sensitivity parameter is defined as the relationship between the deflection signal of the cantilever and the voltage applied to the piezo element. Typically, this parameter is determined in the force plot mode. In order to obtain reliable deflection data, it is essential to calibrate the sensitivity beforehand. The sensitivity of a system can be quantified by determining the slope of the force curve during the period when the cantilever is in contact with the surface of the sample (Bruker, 2010). In order to determine the sensitivity, it is necessary to acquire and display a force curve on a monitor. Subsequently, lines should be drawn within the contact region of the curve and positioned along the slope as depicted in Figure 22 a. Following that click the command menu and choose the option labelled "update sensitivity" as shown in Figure 22 b. Subsequently, make note of the values that are displayed. Afterwards, proceed to apply the mentioned processes to the remaining sensitivity data file and compute the mean value. Then, employ the obtained sensitivity average to the force curve data by manually adjusting the modifying force parameter for each force curve ramp data, hence altering the values of sensitivity and spring constant as shown in the figure 23. All the sensitivity used in this study was shown in the figure 24.
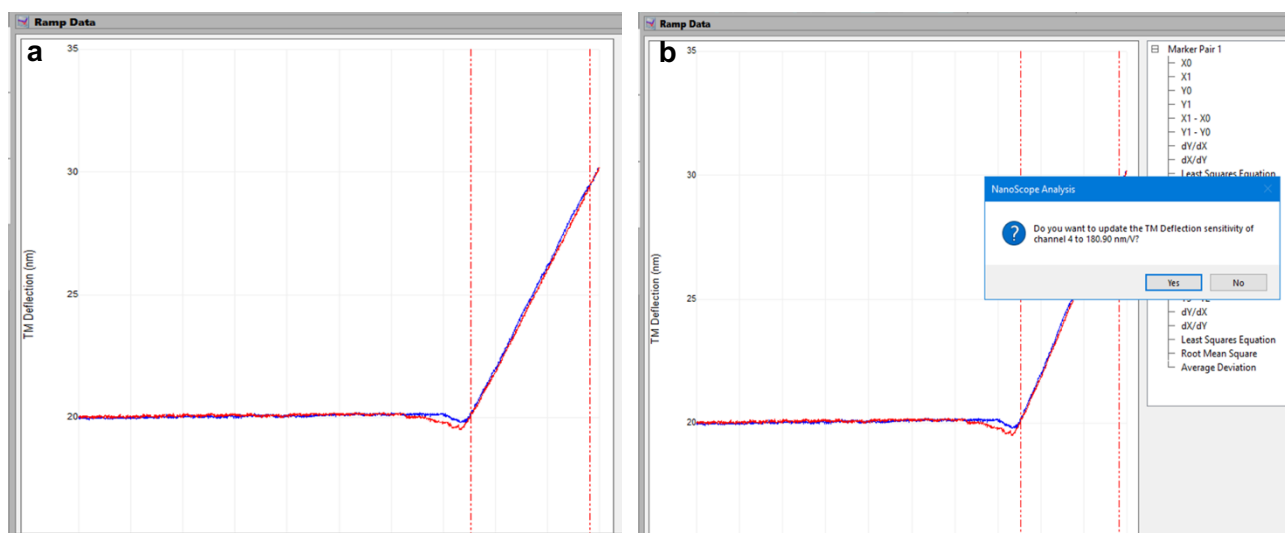
Figure 22. Determining the sensitivity from force curve data by dragging lines between the slope (a) then update the sensitivity from the commands menu (b)
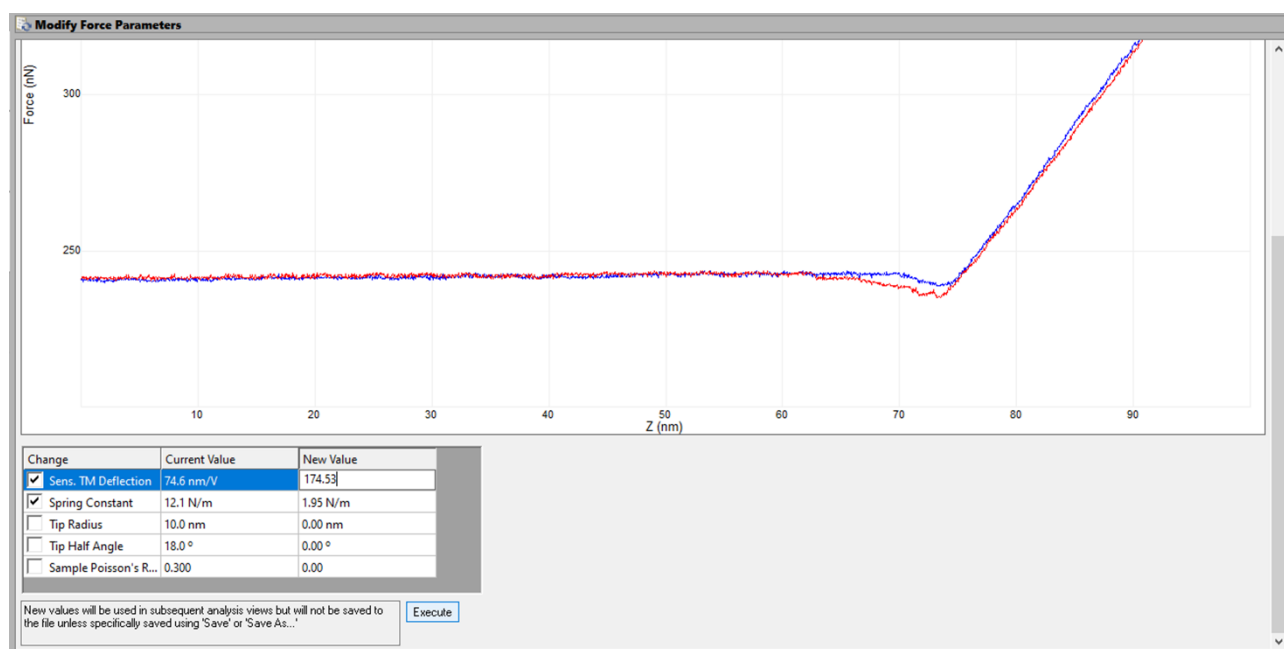
Figure 23. Updating the values of sensitivity and spring constant in modifying force parameter menu

No	Region	Samples Name	Sensitivity (nm/V)	Probe
1	ALT	ALT Human health_mica_12-9-23_sensitivity 0000.0_00006	172.01	1
2	ALT	ALT Human health_mica_12-9-23_sensitivity 0000.0_00007	171.94	1
3	ALT	ALT Human health_mica_12-9-23_sensitivity 0000.0_00008	170.06	1
4	ALT	ALT Human health_mica_12-9-23_sensitivity 0000.0_00056	176.29	1
5	ALT	ALT Human health_mica_12-9-23_sensitivity 0000.0_00057	175.85	1
6	ALT	ALT Human health_mica_12-9-23_sensitivity 0000.0_00058	181.05	1
		Sensitivity Average	**174.5333333**	
1	ALT	ALT deg grade IV 26-9-23.spm0.0_00018	164.56	2
2	ALT	ALT deg grade IV 26-9-23.spm0.0_00022	164.14	2
		Sensitivity Average	**164.35**	
1	ALT	ALT deg grade IV 28-9-23.spm0.0_00021	169.02	2
2	ALT	ALT deg grade IV 28-9-23.spm0.0_00025	169.78	2
		Sensitivity Average	**169.4**	
1	PST	PST healthy human 12-10-23.spm0.0_00017_sensitivity	159.68	3
2	PST	PST healthy human 12-10-23.spm0.0_00021_sensitivity	159.96	3
		Sensitivity Average	**159.82**	
1	PST	PST deg grade 4 human sample 2 1-11-23.spm0.0_00023_sensitivity	146.63	4
2	PST	PST deg grade 4 human sample 2 1-11-23.spm0.0_00027_sensitivity	146.91	4
		Sensitivity Average	**146.77**	

Figure 24. The average sensitivity used for the force curves

Appendix D: AFM Nanoindentation Data

The following results represent the Young's modulus values obtained using nanoindentation using the Hertz model specifically obtained from every individual fibril within all the samples.

ALT degenerated samples

A total of 38 nanoindentations were performed on three separate fibrils from a single sample as depicted in Figure 25. The data points represented by the red values were excluded from the analysis as their corresponding R^2 values were found to be inadequate.

No	Region	File Name	Max Force Fit (%)	Min Force Fit (%)	Young's Modulus (MPa)	R^2
1	ALT degenerated grade 4	ALT Human deg grade 4 _mica_12-9-23_0000.0_00004	39	6	1451	0.9634
2	ALT degenerated grade 4	ALT Human deg grade 4 _mica_12-9-23_0000.0_00005	39	6	2121	0.9127
3	ALT degenerated grade 4	ALT Human deg grade 4 _mica_12-9-23_0000.0_00006	39	6	2816	0.8656
4	ALT degenerated grade 4	ALT Human deg grade 4 _mica_12-9-23_0000.0_00007	39	6	1464	0.895
5	ALT degenerated grade 4	ALT Human deg grade 4 _mica_12-9-23_0000.0_00008	39	6	3017	0.6818
6	ALT degenerated grade 4	ALT Human deg grade 4 _mica_12-9-23_0000.0_00009	39	6	4130	0.9077
7	ALT degenerated grade 4	ALT Human deg grade 4 _mica_12-9-23_0000.0_00010	39	6	2589	0.8818
8	ALT degenerated grade 4	ALT Human deg grade 4 _mica_12-9-23_0000.0_00011	39	6	2310	0.9576
9	ALT degenerated grade 4	ALT Human deg grade 4 _mica_12-9-23_0000.0_00012	39	6	3746	0.8895
10	ALT degenerated grade 4	ALT Human deg grade 4 _mica_12-9-23_0000.0_00013	39	6	3452	0.8591
		Median	**39**	**6**	**2702.5**	**0.89225**

No	Region	File Name	Max Force Fit (%)	Min Force Fit (%)	Young's Modulus (MPa)	R^2
11	ALT degenerated grade 4	ALT deg grade IV 26-9-23.spm0.0_00005	39	6	1300	0.99
12	ALT degenerated grade 4	ALT deg grade IV 26-9-23.spm0.0_00006	39	6	1188	0.9849
13	ALT degenerated grade 4	ALT deg grade IV 26-9-23.spm0.0_00007	39	6	1153	0.9852
14	ALT degenerated grade 4	ALT deg grade IV 26-9-23.spm0.0_00008	39	6	1075	0.9903
15	ALT degenerated grade 4	ALT deg grade IV 26-9-23.spm0.0_00009	39	6	1138	0.9895
16	ALT degenerated grade 4	ALT deg grade IV 26-9-23.spm0.0_00010	39	6	1508	0.9859
17	ALT degenerated grade 4	ALT deg grade IV 26-9-23.spm0.0_00011	39	6	1185	0.9828
18	ALT degenerated grade 4	ALT deg grade IV 26-9-23.spm0.0_00012	39	6	1361	0.9821
19	ALT degenerated grade 4	ALT deg grade IV 26-9-23.spm0.0_00013	39	6	1398	0.9854
20	ALT degenerated grade 4	ALT deg grade IV 26-9-23.spm0.0_00014	39	6	1195	0.9726
21	ALT degenerated grade 4	ALT deg grade IV 26-9-23.spm0.0_00015	39	6	1361	0.9826
22	ALT degenerated grade 4	ALT deg grade IV 26-9-23.spm0.0_00020	39	6	5207	0.8706
23	ALT degenerated grade 4	ALT deg grade IV 26-9-23.spm0.0_00021	39	6	9187	0.7742
24	ALT degenerated grade 4	ALT deg grade IV 26-9-23.spm0.0_00019	39	6	13037	0.4572
		Median	39	6	1300	0.9849
25	ALT degenerated grade 4	ALT deg grade IV 28-9-23.spm0.0_00008	39	6	6101	0.9521
26	ALT degenerated grade 4	ALT deg grade IV 28-9-23.spm0.0_00009	39	6	2837	0.9593
27	ALT degenerated grade 4	ALT deg grade IV 28-9-23.spm0.0_00010	39	6	649	0.9854
28	ALT degenerated grade 4	ALT deg grade IV 28-9-23.spm0.0_00011	39	6	2240	0.9344
29	ALT degenerated grade 4	ALT deg grade IV 28-9-23.spm0.0_00012	39	6	1959	0.9579
30	ALT degenerated grade 4	ALT deg grade IV 28-9-23.spm0.0_00013	39	6	1810	0.9599
31	ALT degenerated grade 4	ALT deg grade IV 28-9-23.spm0.0_00014	39	6	1326	0.9688
32	ALT degenerated grade 4	ALT deg grade IV 28-9-23.spm0.0_00015	39	6	2339	0.9278
33	ALT degenerated grade 4	ALT deg grade IV 28-9-23.spm0.0_00016	39	6	2366	0.9732
34	ALT degenerated grade 4	ALT deg grade IV 28-9-23.spm0.0_00017	39	6	1724	0.9601
35	ALT degenerated grade 4	ALT deg grade IV 28-9-23.spm0.0_00018	39	6	2272	0.8946
36	ALT degenerated grade 4	ALT deg grade IV 28-9-23.spm0.0_00022	39	6	6736	0.9141
37	ALT degenerated grade 4	ALT deg grade IV 28-9-23.spm0.0_00023	39	6	6885	0.8825
38	ALT degenerated grade 4	ALT deg grade IV 28-9-23.spm0.0_00024	39	6	7013	0.817
		Median	39	6	2305.5	0.955

Figure 25. The Young's modulus values for ALT degenerated samples

ALT healthy samples

A total of 36 nanoindentations were performed on three separate fibrils from a single sample as depicted in Figure 26. The data points represented by the red values were excluded from the analysis as their corresponding R^2 values were found to be inadequate.

No	Region	File Name	Max Force Fit (%)	Min Force Fit (%)	Young's Modulus (MPa)	R^2
1	ALT healthy	ALT Human health_mica_12-9-23_0000.0_00009	39	6	1940	0.8896
2	ALT healthy	ALT Human health_mica_12-9-23_0000.0_00010	39	6	2800	0.9529
3	ALT healthy	ALT Human health_mica_12-9-23_0000.0_00011	39	6	1905	0.9625
4	ALT healthy	ALT Human health_mica_12-9-23_0000.0_00012	39	6	2022	0.9472
5	ALT healthy	ALT Human health_mica_12-9-23_0000.0_00013	39	6	1278	0.9106
6	ALT healthy	ALT Human health_mica_12-9-23_0000.0_00014	39	6	1512	0.9249
7	ALT healthy	ALT Human health_mica_12-9-23_0000.0_00015	39	6	2430	0.9424
8	ALT healthy	ALT Human health_mica_12-9-23_0000.0_00016	39	6	1448	0.953
9	ALT healthy	ALT Human health_mica_12-9-23_0000.0_00017	39	6	2120	0.971
10	ALT healthy	ALT Human health_mica_12-9-23_0000.0_00018	39	6	1793	0.9132
11	ALT healthy	ALT Human health_mica_12-9-23_0000.0_00020	39	6	8749	0.8101
12	ALT healthy	ALT Human health_mica_12-9-23_0000.0_00022	39	6	3015	0.9349
13	ALT healthy	ALT Human health_mica_12-9-23_0000.0_00024	39	6	2436	0.8253
14	ALT healthy	ALT Human health_mica_12-9-23_0000.0_00025	39	6	3408	0.8784
15	ALT healthy	ALT Human health_mica_12-9-23_0000.0_00026	39	6	3477	0.6512
16	ALT healthy	ALT Human health_mica_12-9-23_0000.0_00027	39	6	2561	0.8947
17	ALT healthy	ALT Human health_mica_12-9-23_0000.0_00028	39	6	2065	0.8075
18	ALT healthy	ALT Human health_mica_12-9-23_0000.0_00030	39	6	6950	0.7236
19	ALT healthy	ALT Human health_mica_12-9-23_0000.0_00031	39	6	5755	0.7102
20	ALT healthy	ALT Human health_mica_12-9-23_0000.0_00032	39	6	0	0
21	ALT healthy	ALT Human health_mica_12-9-23_0000.0_00029	39	6	3062	0.03831
		Median	39	6	2430	0.9106
22	ALT healthy	ALT Human health_mica_12-9-23_0000.0_00037	39	6	1722	0.9595
23	ALT healthy	ALT Human health_mica_12-9-23_0000.0_00038	39	6	1851	0.9175
24	ALT healthy	ALT Human health_mica_12-9-23_0000.0_00039	39	6	1923	0.9183
25	ALT healthy	ALT Human health_mica_12-9-23_0000.0_00040	39	6	1717	0.9619
26	ALT healthy	ALT Human health_mica_12-9-23_0000.0_00041	39	6	1684	0.8776
27	ALT healthy	ALT Human health_mica_12-9-23_0000.0_00042	39	6	1974	0.9286
28	ALT healthy	ALT Human health_mica_12-9-23_0000.0_00043	39	6	1912	0.9272
		Median	39	6	1851	0.9272
29	ALT healthy	ALT Human health_mica_12-9-23_0000.0_00047	39	6	1551	0.8683
30	ALT healthy	ALT Human health_mica_12-9-23_0000.0_00048	39	6	1534	0.888
31	ALT healthy	ALT Human health_mica_12-9-23_0000.0_00049	39	6	1258	0.8201
32	ALT healthy	ALT Human health_mica_12-9-23_0000.0_00050	39	6	1368	0.8559
33	ALT healthy	ALT Human health_mica_12-9-23_0000.0_00051	39	6	1531	0.8575
34	ALT healthy	ALT Human health_mica_12-9-23_0000.0_00052	39	6	1632	0.8328
35	ALT healthy	ALT Human health_mica_12-9-23_0000.0_00053	39	6	3714	0.6075
36	ALT healthy	ALT Human health_mica_12-9-23_0000.0_00054	39	6	3046	0.4522
		Median	39	6	1534	0.8559

Figure 26. The Young's modulus values for ALT healthy samples

PST healthy samples

A total of 13 nanoindentations were performed on a single sample as depicted in Figure 27. The data points represented by the red values were excluded from the analysis as their corresponding R^2 values were found to be inadequate.

No	Region	File Name	Max Force Fit (%)	Min Force Fit (%)	Young's Modulus (MPa)	R^2
1	PST healthy	PST healthy human 12-10-23.spm0.0_00006	39	6	1209	0.9836
2	PST healthy	PST healthy human 12-10-23.spm0.0_00007	39	6	1134	0.9828
3	PST healthy	PST healthy human 12-10-23.spm0.0_00008	39	6	1148	0.9922
4	PST healthy	PST healthy human 12-10-23.spm0.0_00009	39	6	1916	0.9871
5	PST healthy	PST healthy human 12-10-23.spm0.0_00010	39	6	1029	0.9847
6	PST healthy	PST healthy human 12-10-23.spm0.0_00011	39	6	980	0.9891
7	PST healthy	PST healthy human 12-10-23.spm0.0_00012	39	6	1041	0.9837
8	PST healthy	PST healthy human 12-10-23.spm0.0_00013	39	6	1174	0.9869
9	PST healthy	PST healthy human 12-10-23.spm0.0_00014	39	6	1029	0.9904
10	PST healthy	PST healthy human 12-10-23.spm0.0_00015	39	6	952	0.99
11	PST healthy	PST healthy human 12-10-23.spm0.0_00019	39	6	4011	0.9353
12	PST healthy	PST healthy human 12-10-23.spm0.0_00018	39	6	14057	0.5997
13	PST healthy	PST healthy human 12-10-23.spm0.0_00020	39	6	11089	0.3977
		Median	39	6	1134	0.9869

Figure 27. The Young's modulus values for PST healthy samples

PST degenerated samples

A total of 17 nanoindentations were performed on a single sample as depicted in Figure 28. The data points represented by the red values were excluded from the analysis as their corresponding R^2 values were found to be inadequate.

No	Region	File Name	Max Force Fit (%)	Min Force Fit (%)	Young's Modulus (MPa)	R^2
1	PST degenerated	PST deg grade 4 human sample 2 1-11-23.spm0.0_00006	39	6	2311	0.6442
2	PST degenerated	PST deg grade 4 human sample 2 1-11-23.spm0.0_00008	39	6	2655	0.6936
3	PST degenerated	PST deg grade 4 human sample 2 1-11-23.spm0.0_00009	39	6	3236	0.6226
4	PST degenerated	PST deg grade 4 human sample 2 1-11-23.spm0.0_00010	39	6	3812	0.8853
5	PST degenerated	PST deg grade 4 human sample 2 1-11-23.spm0.0_00011	39	6	2652	0.8573
6	PST degenerated	PST deg grade 4 human sample 2 1-11-23.spm0.0_00012	39	6	3170	0.7525
7	PST degenerated	PST deg grade 4 human sample 2 1-11-23.spm0.0_00013	39	6	3123	0.6302
8	PST degenerated	PST deg grade 4 human sample 2 1-11-23.spm0.0_00014	39	6	3672	0.8588
9	PST degenerated	PST deg grade 4 human sample 2 1-11-23.spm0.0_00015	39	6	3445	0.6808
10	PST degenerated	PST deg grade 4 human sample 2 1-11-23.spm0.0_00016	39	6	3227	0.7976
11	PST degenerated	PST deg grade 4 human sample 2 1-11-23.spm0.0_00017	39	6	2829	0.6365
12	PST degenerated	PST deg grade 4 human sample 2 1-11-23.spm0.0_00018	39	6	1865	0.8652
13	PST degenerated	PST deg grade 4 human sample 2 1-11-23.spm0.0_00019	39	6	1442	0.8484
14	PST degenerated	PST deg grade 4 human sample 2 1-11-23.spm0.0_00007	39	6	1896	0.5836
15	PST degenerated	PST deg grade 4 human sample 2 1-11-23.spm0.0_00024	39	6	0	0
16	PST degenerated	PST deg grade 4 human sample 2 1-11-23.spm0.0_00025	39	6	34	0
17	PST degenerated	PST deg grade 4 human sample 2 1-11-23.spm0.0_00026	39	6	0	0
		Median	39	6	3123	0.7525

Figure 28. The Young's modulus values for PST degenerated samples

Appendix E: D-banding

This figure 29 shows the D-banding values for all the samples.

The D-banding measured of the individual fibrils
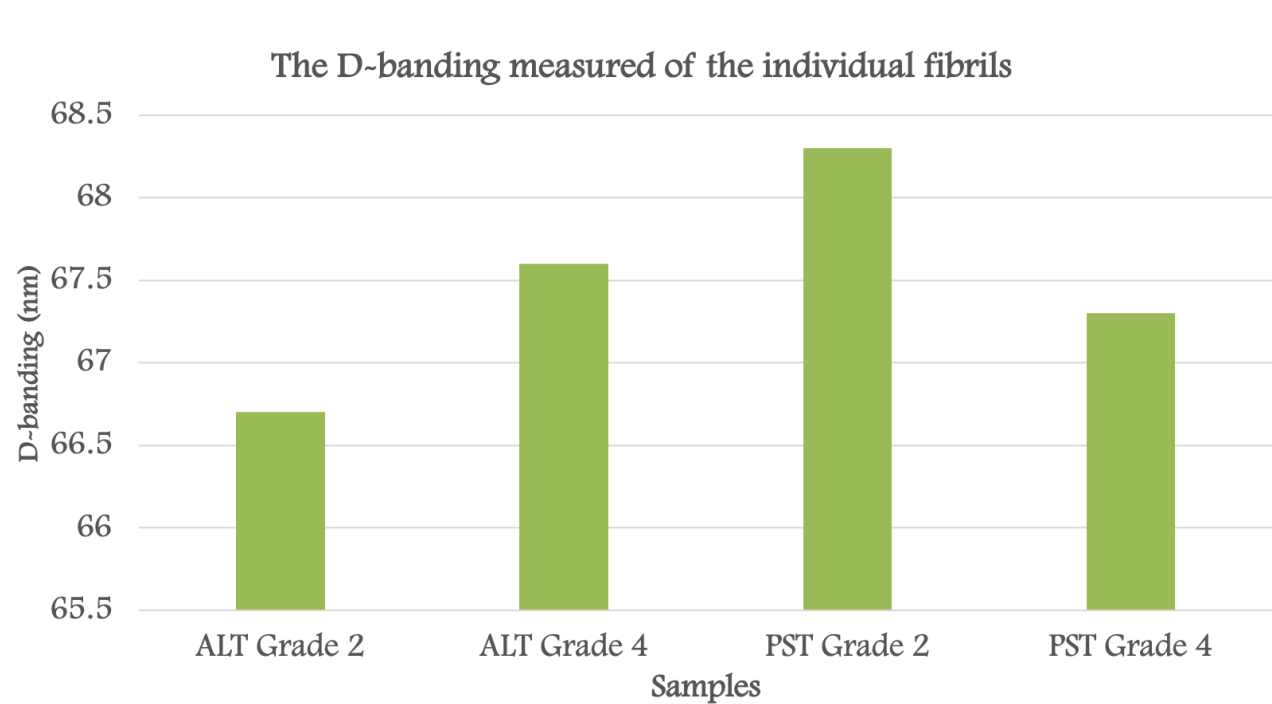
Figure 29. The D-banding values for all the samples